Strongly coupled piezoelectric cantilevers for broadband vibration energy harvesting

David Gibus, Pierre Gasnier, Adrien Morel, Fabien Formosa, Ludovic Charleux, Sébastien Boisseau, Gaël Pillonnet, Carlos Augusto Berlitz, Anthony Quelen, Adrien Badel

Strongly Coupled Piezoelectric Cantilevers for Broadband Vibration Energy Harvesting

David Gibus[1,2], Pierre Gasnier[1], Adrien Morel[1,2], Fabien Formosa[2], Ludovic Charleux[2], Sébastien Boisseau[1], Gaël Pillonnet[1], Carlos Augusto Berlitz[1], Anthony Quelen[1], Adrien Badel[2,*]

[1]Université Grenoble Alpes, CEA, LETI, MINATEC, F-38000 Grenoble, France
[2]SYMME, Université Savoie Mont-Blanc, F-74000, Annecy, France

[*]Corresponding author.
E-mail address: adrien.badel@univ-smb.fr

Abstract

Vibration energy harvesters based on piezoelectric resonators are promising for powering Wireless Sensors Nodes (WSNs). Yet, any mismatch between the resonant frequency of traditional harvesters and the vibration frequency can drastically decrease the scavenged power and make them ineffective. Electrical techniques able to tune the resonant frequency of piezoelectric harvesters has been proposed as a solution and opens up new perspectives. To be fully competitive, this approach requires energy harvesters with very strong global electromechanical coupling coefficients k^2 (>10%), whose design remains a challenge today. This work reports on a method to design strongly coupled piezoelectric cantilevers thanks to an analytical approach based on the Rayleigh-Ritz method and a two degrees-of-freedom model, which considers the proof mass inertia effects. Through an expression of the coupling coefficient, we provide design guidelines, which are experimentally validated. We show that a long proof mass is a very effective configuration to maximize the global electromechanical coupling coefficient and consequently the frequency bandwidth of the system. Three proposed prototypes exhibit some of the strongest squared global electromechanical coupling coefficients k^2 of the state-of-the-art of piezoelectric harvesters (16.6% for the PMN-PT cantilever, 11.3% and 16.4% for the narrow and wide PZT-5A cantilevers respectively) and demonstrate a wide bandwidth behavior (10.1%, 7.8% and 11.3% of the central frequency respectively). Using a strongly coupled prototype based on PZT-5A leveraged by a dedicated integrated circuit, we experimentally show that it can harvest enough power (more than 100µW) to supply a WSN over a frequency bandwidth as large as 21%.

1. Introduction

Ambient energy harvesting appears as a relevant technology to supply sensors where batteries cannot be used or need to be complemented [1]. In environments with no obvious light or thermal sources, vibration energy harvesting is an interesting strategy for which piezoelectric-based resonators are attractive for their high power density at small scale [2]. However, because a mismatch between the harvester resonant frequency and the vibration frequency of the host structure makes them inefficient, the narrow frequency bandwidth of vibration energy harvesters is still an important issue [3]. This mismatch can be caused by the variation of the dominant frequency of the vibration source while the resonant frequency of the harvester remains constant. This situation is encountered in many applications as shown by Rantz and Roundy [5]: one third of the vehicle vibration signals presented in the NiPS Laboratory "Real Vibration" database [4] exhibit a dominant vibration frequency that varies. This mismatch can also occur when the resonant frequency of the harvester drifts due to the aging of materials and assemblies [6] or temperature variations of the environment [7,8]. In response to these frequency mismatches a new trend has recently emerged with the development of electrical techniques [9,10] and power management

circuits [11,12] able to tune the resonant frequency of piezoelectric cantilevers thanks to the coupling effect between the mechanical dynamics and the electrical circuit. For that purpose, the design and the fabrication of piezoelectric harvesters exhibiting a very strong global electromechanical coupling coefficient k are mandatory and open up promising perspectives for broadband vibration energy harvesting, but a systematic model for optimizing piezoelectric cantilevers with a long proof mass is missing in the state of the art [13]. This paper proposes an analytical study corroborated by experimental results to give general guidelines on the geometrical and material parameters that influence the cantilever's k^2 in order to maximize it.

Although nonlinear or bistable mechanical harvesters are effective in overcoming the narrow bandwidth limitation of classical resonator-based vibration energy harvester, they are dependent on the input amplitude [14,15], and multi-degree of freedom harvesters suffer from low power densities [16]. Only a small tuning range could be achieved in the early stages of resonant frequency tuning by electrical methods [17], but recent works in the field make them increasingly interesting for broadband vibration energy harvesting. In 2018, Cai and Manoli [11] from IMTEK managed to achieve a bandwidth of 9.0% with an enhanced Synchronous Electric Charge Extraction (SECE) electrical interface and, in 2019, Zhao *et al*. [18] reached a bandwidth of 6.9% with a non-linear electrical technique coupled to a PZT-5H based cantilever ($k^2 = 6.5\%$). Despite their interesting achievements, the two above-mentioned works used commercial cantilevers that have moderate electromechanical coupling coefficients and low quality factors. They did not present any optimized prototype and, even though the presented electrical methods have a substantial influence, their remarkable bandwidths are partly due to the low quality factor of the harvesters, which leads to low power density solutions.

Strongly coupled energy harvesters have been considered as a solution to further extend the frequency bandwidth. Ahmed-Seddik *et al.* [19] proposed a tapered cantilever ($k^2 = 49.3\%$) using the 33-mode of the PZN-PT material associated to a resonant frequency tuning technique based on tunable resistances and capacitances, to reach 32.7% of frequency bandwidth [20]. However, no modeling was proposed and compared to experiments. In addition, the structure showed a low quality factor and its complex assembly procedure made it inadequate for industrial processes. Later on, Badel and Lefeuvre [21] introduced a strongly coupled PZN-PT-based cantilever with a long proof mass that could theoretically reach a bandwidth of 45% when associated with the Frequency Tunable SECE (FT-SECE) technique. Their device exhibited interesting performances ($k^2 = 53\%$) while it was based on a very simple mechanical configuration. Despite the absence of an optimization method, this outstanding result places the cantilevers with a long proof mass as a competitive structure for designing strongly coupled harvesters. This statement was partially explained by Kim *et al.* [22], which showed that using long proof masses tends to homogenize the strain distribution along the beam, but no optimization method nor obvious explanation regarding the global electromechanical coupling coefficient and the bandwidth were mentioned. It is also worth noting that the aforementioned wide bandwidths were obtain with relaxor-based ferroelectric single crystals having very low temperature resistance compared to piezoelectric ceramics and being difficult and expensive to produce industrially at the moment [23]. In this paper, we provide an analysis concerning both single crystal-based harvesters and ceramic-based harvesters.

To date, a few works have studied the optimization of cantilevers with a proof mass. In 2014, Xiong *et al.* [24] discussed the optimization of their electromechanical coupling coefficient using a model associated with FEM simulations. Though they limited their analysis to cubic proof masses, they revealed that piezoelectric patches must cover the entire length of the beam when a proof mass is used. Under this condition, the proof mass could increase the squared global electromechanical coupling k^2 by more than 10% compared to the case without proof mass. In 2016, Jia *et al.* [25] analyzed the influence of the proof mass length on the harvested power thanks to a model associated with FEM simulations and 4 prototypes. They conclude that, within the linear response, the generated power is maximal for proof masses occupying 60%-70% of the total cantilever length. More recently, in 2019, Pradeesh and Udhayakumar [13] revealed, through FEM simulations of unimorph cantilevers with moderate proof mass sizes, that the shape of the proof mass has a minimal effect on the power harvested relative to its mass. Although these works provide interesting results, none of them is based on a comprehensive analytical study corroborated by experiments.

So far, some works have analytically optimized the electromechanical coupling coefficients of piezoelectric cantilevers without proof mass using the Single Degree of Freedom (SDOF) model [18,26]. Though the SDOF model is commonly-used for cantilevers using a localized tip proof mass [27], it proved to be inaccurate for a bulky proof mass [28,29]. Other analytical attempts to better account for the effects induced by the proof mass either do not consider the rotary inertia [30] or still show significant discrepancies when compared to 2D Finite Element Method (FEM) simulations [31]. To the authors knowledge, analytical results detailing the impact of the proof mass on k^2, and thus on the frequency bandwidth, have never been proposed in the state of the art.

In this paper, we present a method based on an analytical modeling approach to design strongly coupled piezoelectric cantilevers with large proof masses in the purpose of frequency tuning for vibration energy harvesting. In the first section, we underline the interest of increasing the global coupling coefficient of a piezoelectric harvester to improve the frequency bandwidth using a classical single degree of freedom model. Then, by using the Rayleigh-Ritz energy method and determining the cantilever modes shapes from a two degree of freedom (2-DOF) model, we propose a novel analytical expression of the alternative electromechanical coupling coefficient $k_e^2 = k^2/(1-k^2)$. We then use this expression in section 3 to analyze the geometrical and material parameters effects on k_e^2. As a result, we design three different strongly coupled harvesters integrating long proof masses and involving two types of piezoelectric materials: PMN-PT single crystal and PZT ceramic. For the PZT material, a narrow and a wide cantilever are evaluated to analyze the evolution of k^2 with respect to the beam geometry. Experiments and results are detailed and discussed in section 4. In particular, we discuss the validation of the proposed model and the comparison of the performance of the prototypes with the state of the art. Finally, we experimentally demonstrate that we can dynamically track the ambient vibration central frequency thanks to a strongly coupled piezoelectric harvester whose resonant frequency is tuned thanks to a previously developed integrated circuit that embeds a self-powered maximum power point tracking algorithm [12].

2. Analytical modeling

2.1. Advantages of a strong global coupling coefficient

Around one of its resonant frequency, a piezoelectric cantilever can be accurately modeled by a SDOF system as expressed in (1) [22].

$$\begin{cases} M\ddot{r} + C\dot{r} + Kr - \Theta v = -B_f \ddot{w}_B \\ \Theta\dot{r} + C_p\dot{v} + i = 0 \end{cases} \quad (1)$$

In which M, K, C are the system's equivalent inertial mass, stiffness and viscous damping coefficient. Θ, C_p, and B_f are the coupling term, the piezoelectric clamped capacitance and the forcing term respectively. r, v and i are the generalized spatial coordinate, the output voltage and current respectively. $\ddot{w}_b$ is the acceleration of the base (clamped-end) of the beam.

The short circuit and open circuit resonant angular frequencies ω_1^{sc} and ω_1^{oc} are expressed by (2) and (3) where k_e is the alternative electromechanical coupling coefficient of the system and is given in (4). k_e^2 can be directly calculated from the square of the global electromechanical coupling coefficient k^2. The viscous damping term can be expressed as a function of the mechanical damping ratio ζ_m or the mechanical quality factor Q_m (5).

$$\omega_1^{sc} = \sqrt{\frac{K}{M}} \quad (2) \qquad \omega_1^{oc} = \omega_1^{sc}\sqrt{1+k_e^2} \quad (3)$$

$$k_e^2 = \frac{k^2}{1-k^2} = \frac{\Theta^2}{KC_p} \quad (4) \qquad C = 2\zeta_m M\omega_1^{sc} = \frac{M\omega_1^{sc}}{Q_m} \quad (5)$$

The expression of the RMS output power P can be found in [32] as a function the equivalent parameters and the angular frequency. Using the normalization given in [33] (expressed in (6)), the Figure 1 shows the normalized power P' when considering an optimal resistive load, as a function of the normalized pulsation Ω (see equation (7) where ω is the excitation pulsation). The normalized power P' allows us to study the harvesters' performance independently of their resonant frequencies, inertial masses and forcing acceleration magnitude.

$$P' = P\frac{8M\omega_1^{sc}}{B_f^2|\ddot{w}_b|^2} \leq Q_m \quad (6) \qquad \Omega = \frac{\omega}{\omega_1^{sc}} \quad (7)$$

For the systems that have sufficiently large k_e^2 and Q_m ($k_e^2 Q_m \geq 2$), P' shows, for optimal resistive loads (R), two maxima ($P'_{max} = Q_m$) separated by a less interesting low in the curve which can be raised thanks to optimal combinations of resistance and capacitance loads (R and C) [34] (Figure 1). Because banks of capacitors cannot

be easily integrated in a circuit, strategies that involve non-linear electrical techniques [35] have recently been developed to optimize the harvested power in the $[\omega_1^{sc}, \omega_1^{oc}]$ bandwidth and even beyond with the SC-SECE [10] and the FT-SECE [9] techniques. Consequently, we define the target bandwidth of a strongly coupled harvester as:

$$\frac{\Delta\Omega}{\Omega_c} = \frac{\Omega_H - \Omega_L}{\Omega_c} \tag{8}$$

Where Ω_L and Ω_H are defined at half of the maximal power (Figure 1) and Ω_c is the normalized central pulsation given by $(\Omega_L + \Omega_H)/2$.

Figure 2 shows the maximal normalized power P'_{max} and the frequency bandwidth as a function of k^2 for various quality factors. It can be deduced that increasing k^2 beyond a certain value does not show any interest for increasing the maximal power. Though, higher k^2 significantly improves the bandwidth. Optimizing the global coupling coefficient is thus an effective solution to broaden the harvesting frequency bandwidth. In this way, this work proposes the development of a generic model aiming at the maximization of the global electromechanical coupling coefficient of piezoelectric cantilevers well suited for frequency tuning applications.

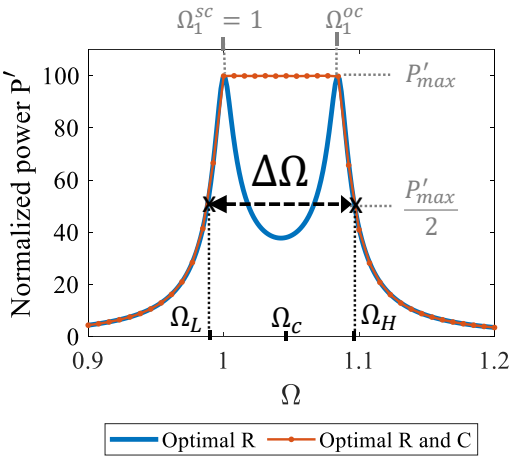

Figure 1: Normalized power as a function of the normalized pulsation for $k^2 = 15\%$ and $Q_m = 100$.

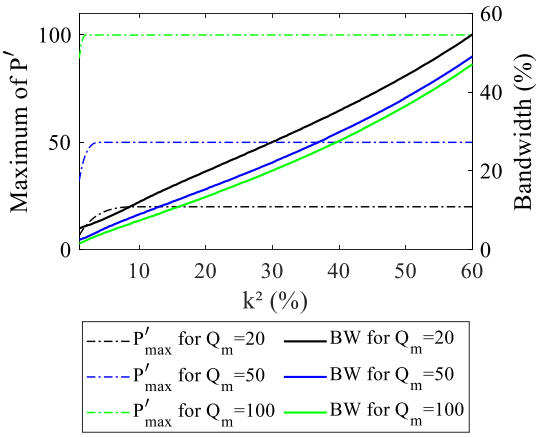

Figure 2: Maximal normalized power and bandwidth (BW) as a function of k^2 for optimal R and C loads.

2.2. Problem definition and modeling strategy

The proposed harvester design relies on a bimorph cantilever with a bulky proof mass at tip end (Figure 3.a) and for which the two piezoelectric layers (PL) share the same length as the substrate (central layer). As it will be detailed in the following, a proof mass having a high rotary inertia favors the homogenization of the strain distribution within the PL. For that reason, it is optimal to choose a same length for the substrate and the PL. The PL have the same thicknesses (h_p) and are entirely covered by electrodes at the bottom and the top surfaces, which are connected in parallel (Figure 4). Figure 3.b depicts the proposed cantilever during bending. A proof mass of any shape can be considered since we can model it with an equivalent point mass defined by a mass M_t and a rotary inertia I_t at a distance D_t from the "free" end of the beam on the neutral axis. Without loss of generality, in the following, we consider a symmetric proof mass with respect to the neutral axis of the beam that has the same width B as the beam. If the center of gravity of the mass is not on the neutral axis along the z-axis, the related distance would have to be taken into account in I_t as detailed in appendix A.

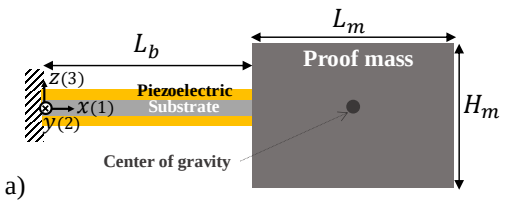

a)

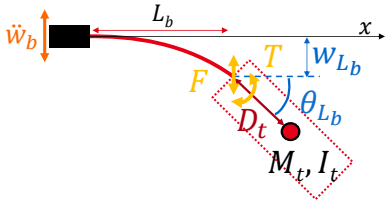

b)

Figure 3: a) Cantilever with a proof mass and b) cantilever during bending.

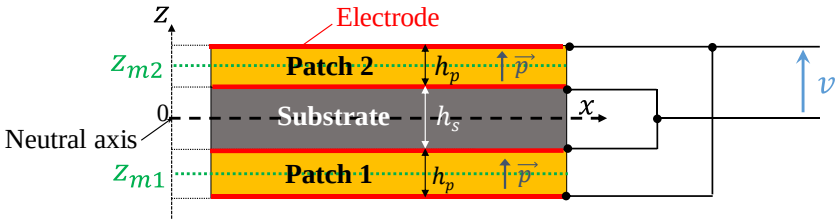

Figure 4: Beam layers and electrodes connection in parallel

Here, we use the Rayleigh-Ritz method associated to a 2-DOF analytical model. The Rayleigh-Ritz method is commonly used for modeling vibrating structures and its application on piezoelectric devices has been firstly presented in [36] and has lately been detailed in [22] and [32] for piezoelectric cantilevers with a proof mass. Such an approach allows to reduce the analysis to a multi-degree of freedom system around the resonant frequencies of the device. However, in these former works, the electric field was considered constant according to the z-direction in the piezoelectric material, which leads to non-negligible errors for strongly coupled structures [37]. Therefore, an improvement of the modeling method is proposed in section 2.3, considering a variable electric field through the thickness of the piezoelectric patches.

As the expressions of the vibration mode shapes are required for the Rayleigh-Ritz method, we determine (section 2.4) the analytical expressions of the two first bending mode shapes considering a 2-DOF model. Then, we deduce (section 2.5) the equivalent parameters of a 2-DOF system based on the Rayleigh-Ritz method from these resulting vibration mode shapes. Reducing the analysis to the first resonant mode, we are then able to determine an analytical expression for the square of the alternative electromechanical coupling coefficient k_e^2.

2.3. Rayleigh-Ritz method

The Hamilton principle [36] is applied to the structure (9). The virtual variations of the kinetic energy T_k, the internal electrical energy W_e, the potential energy U and the external work W are null between times t_1 and t_2. In equations (12) to (15), the energy terms and the external work are deduced from the linear constitutive relations of piezoelectricity (10) and the Hooke law (11) ([38,39]).

$$\int_{t_1}^{t_2} [\delta(T_k - U + W_e) + \delta W)]dt = 0 \tag{9}$$

$$\begin{pmatrix} \boldsymbol{T} \\ \boldsymbol{D} \end{pmatrix} = \begin{bmatrix} \boldsymbol{c^E} & -\boldsymbol{e^t} \\ \boldsymbol{e} & \boldsymbol{\varepsilon^S} \end{bmatrix} \begin{pmatrix} \boldsymbol{S} \\ \boldsymbol{E} \end{pmatrix} \tag{10}$$

$$\boldsymbol{T} = \boldsymbol{c_s S} \tag{11}$$

$$T_k = \frac{1}{2}\left[m \int_0^{L_b} (\vec{\boldsymbol{z}}\dot{w})^t (\vec{\boldsymbol{z}}\dot{w})\, dx + M_t \left(\vec{\boldsymbol{z}}\left(\dot{w}_{L_b} + D_t \dot{w}'_{L_b}\right)\right)^t \left(\vec{\boldsymbol{z}}\left(\dot{w}_{L_b} + D_t \dot{w}'_{L_b}\right)\right) + I_t \left(\vec{\boldsymbol{y}}\dot{w}'_{L_b}\right)^t \left(\vec{\boldsymbol{y}}\dot{w}'_{L_b}\right) \right] \tag{12}$$

$$U = \frac{1}{2}\left[\int_{\mathcal{V}_s} \boldsymbol{S}^t \boldsymbol{c_s} \boldsymbol{S} d\mathcal{V}_s + \int_{\mathcal{V}_p} \boldsymbol{S}^t \boldsymbol{c^E} \boldsymbol{S} d\mathcal{V}_p - \int_{\mathcal{V}_p} \boldsymbol{S}^t \boldsymbol{e^t} \boldsymbol{E} d\mathcal{V}_p \right] \tag{13}$$

$$W_e = \frac{1}{2}\left[\int_{\mathcal{V}_p} \boldsymbol{E}^t \boldsymbol{e} \boldsymbol{S} d\mathcal{V}_p + \int_{\mathcal{V}_p} \boldsymbol{E}^t \boldsymbol{\varepsilon^S} \boldsymbol{E} d\mathcal{V}_p \right] \tag{14}$$

$$\delta W = \int_0^{L_b} (\vec{\boldsymbol{z}}\delta w).(-m\vec{\boldsymbol{z}}\ddot{w}_B) dx + \left(\vec{\boldsymbol{z}}\delta\left(w_{L_b} + D_t w'_{L_b}\right)\right).(-M_t \vec{\boldsymbol{z}}\ddot{w}_B) + v.q \tag{15}$$

$$m = B(h_s \rho_s + 2h_p \rho_p) \tag{16}$$

Where $\boldsymbol{E}$, $\boldsymbol{S}$, $\boldsymbol{D}$ and $\boldsymbol{T}$ are the components of the electric field, strain, electric displacement and stress respectively. In equations (12) to (15) the superscript $(\,)^t$ denotes transpose.

$\boldsymbol{e}$ is the piezoelectric constant matrix, $\boldsymbol{\epsilon^S}$ is the dielectric matrix at constant strain, $\boldsymbol{c^E}$ is the elastic stiffness matrix of the piezoelectric material at null electric field and $\boldsymbol{c_s}$ is the elastic stiffness matrix of the substrate material. m is the mass per unit of length of the beam (substrate and piezoelectric layers) defined in (16) where ρ_p and ρ_s are densities of the piezoelectric material and the substrate respectively.

$\vec{\boldsymbol{z}}$ and $\vec{\boldsymbol{y}}$ are unitary vectors in the O_z and O_y directions respectively ($\vec{\boldsymbol{z}} = [0; 0; 1]$ and $\vec{\boldsymbol{y}} = [0; 1; 0]$).

As only the bending of the beam is considered, the relative displacement is reduced to the transverse (*z* direction) deflection of the beam relative to its base: $w(x,t)$. $w_{L_b}(t)$ is the displacement at the end of the beam $w(L_b,t)$. The apostrophes represent the spatial derivative. Since small deformations are considered, $w'_{L_b}(t)$ is then the rotation at the end of the beam.

The external work W is due to the applied mechanical excitation and the electrical charge extraction. The mechanical work comes from the inertial load due to the base excitation $\ddot{w}_b(t)$.

As the bimorph is symmetric and the electrodes are connected in parallel, the voltage v is equal for both patches and the total charge q is equal to the sum of the charge extracted from each patch. We define v as the generalized electrical voltage coordinate.

Using the Rayleigh–Ritz approach, $w(x,t)$ can be expressed as the sum of n_r individual modes shapes $\phi_i(x)$ multiplied by a generalized mechanical coordinate $r_i(t)$ as given in (17). $\boldsymbol{\phi_r}(x)$ is a row vector of mode shapes $[\phi_1(x), \phi_2(x), ..]$ and $\boldsymbol{r}(t)$ is the column vector of the $r_i(t)$.

$$w(x,t) = \sum_{i=1}^{n_r} \phi_i(x) r_i(t) = \boldsymbol{\phi_r}(x)\boldsymbol{r}(t) \tag{17}$$

As the beam length is much larger compared to its thickness ($L_b > 10\ (2h_p + h_s)$), the Euler-Bernoulli theory can be used. Therefore, the axial strain components are only related to bending. The axial strain at the distance *z* from the neutral axis is then proportional to its curvature at that position x, as written in (18).

$$S_1(x,y,z,t) = -z\frac{\partial^2 w(x,t)}{\partial x^2} \tag{18}$$

For the 1D beam modeling, we assume no stress in the *z* direction in the structure and one of the two following assumptions has to be considered for the out-of-plane stress:

i) plane stress assumption is used for narrow beams ($B/L_b < 0.2$) as no stress is considered in the out-of-plane direction (O_y),

ii) plane strain assumption is used for wide beams ($B/L_b > 5$) as no strain is considered in the out-of-plane direction.

We thus express the strain-stress relations in the substrate beam and the piezoelectric materials thanks to the Hooke law (19) and the in-plane piezoelectric constitutive equations (20) and (21). Because of the electrodes architecture, the displacement field $\boldsymbol{D}$ and the electric field $\boldsymbol{E}$ are only considered in the transverse direction ($\boldsymbol{D} = D_3\vec{\boldsymbol{z}}$ and $\boldsymbol{E} = E_3\vec{\boldsymbol{z}}$).

$$T_1^S = Y_s^{ef} S_1 \tag{19}$$

$$\begin{cases} T_1^p = c_{11}^{ef} S_1 - e_{31}^{ef} E_3 & (20) \\ D_3 = e_{31}^{ef} S_1 + \epsilon_{33}^{ef} E_3 & (21) \end{cases}$$

T_1^p, D_3, E_3 are the longitudinal stress, the transverse displacement field and the transverse electric field respectively. c_{11}^{ef}, e_{31}^{ef}, ϵ_{33}^{ef} are the effective piezoelectric coefficients and Y_s^{ef} is the effective Young modulus obtained according to the given plane stress or plane strain consideration. Y_s^{ef} is obtained from the Young modulus Y_s and the Poisson ratio ν for isotropic materials (22). The piezoelectric effective coefficients are deduced from the piezoelectric matrix $\boldsymbol{d}$, the compliance matrix $\boldsymbol{s^E}$ and the free dielectric matrix $\boldsymbol{\epsilon^T}$ (with $\boldsymbol{e} = \boldsymbol{d}\boldsymbol{s^E}^{-1}$, $\boldsymbol{c^E} = \boldsymbol{s^E}^{-1}$ and $\boldsymbol{\epsilon^S} = \boldsymbol{\epsilon^T} - \boldsymbol{d}\boldsymbol{s^E}^{-1}\boldsymbol{d^t}$) in equations (23) to (25).

$$Y_s^{ef} = \begin{cases} Y_s & \text{plane stress} \\ \dfrac{Y_s}{1-\nu^2} & \text{plane strain} \end{cases} \quad (22) \qquad \epsilon_{33}^{ef} = \begin{cases} \epsilon_{33}^T - \dfrac{d_{31}^2}{s_{11}^E} & \text{plane stress} \\ \epsilon_{33}^T + \dfrac{s_{22}^E d_{31}^2 - 2\, d_{31} d_{32} s_{12}^E + s_{11}^E d_{32}^2}{{s_{12}^E}^2 - s_{11}^E s_{22}^E} & \text{plane strain} \end{cases} \quad (23)$$

$$c_{11}^{ef} = \begin{cases} \dfrac{1}{s_{11}^E} & \text{plane stress} \\ \dfrac{s_{22}^E}{s_{22}^E s_{11}^E - {s_{12}^E}^2} & \text{plane strain} \end{cases} \quad (24) \qquad e_{31}^{ef} = \begin{cases} \dfrac{d_{31}}{s_{11}^E} & \text{plane stress} \\ \dfrac{s_{22}^E d_{31} - d_{32} s_{12}^E}{s_{22}^E s_{11}^E - {s_{12}^E}^2} & \text{plane strain} \end{cases} \quad (25)$$

By reusing the strategy proposed in [37] for piezoelectric actuators, here, we write the electric field and the longitudinal stress in equations (26) and (27) for a piezoelectric layer n (with $n \in [1,2]$).

$$E_3^n = (-1)^{n+1} \frac{v(t)}{h_p} + \frac{e_{31}^{ef}}{\epsilon_{33}^{ef}} (z - z_{mn}) \frac{\partial^2 w(x,t)}{\partial x^2} \quad (26)$$

$$T_1^{P_n} = c_{11}^{ef} \left(-z \frac{\partial^2 w(x,t)}{\partial x^2} - k_{31e}^2 (z - z_{mn}) \frac{\partial^2 w(x,t)}{\partial x^2} \right) + (-1)^n e_{31}^{ef} \frac{v(t)}{h_p} \quad (27)$$

For a symmetric bimorph, z_{mn} is the center position of each piezoelectric patch along the z-axis (Figure 4): $z_{m1} = -(h_p + h_s)/2$ and $z_{m2} = (h_p + h_s)/2$. $k_{e_{31}}^2$, defined in (28), is the squared expedient electromechanical coupling coefficient of the piezoelectric material. As both k_{31}^2 and $k_{e_{31}}^2$ depend on the effective piezoelectric coefficients, they vary according to the given plane stress or plane strain assumption.

$$k_{e_{31}}^2 = \frac{k_{31}^2}{1 - k_{31}^2} = \frac{{e_{31}^{ef}}^2}{c_{11}^{ef} \epsilon_{33}^{ef}} \quad (28)$$

By substituting the displacement (17), the strain (18) and the electric field expressions (26) in the energy conservation equation (10) and by integrating by parts, we can deduce the multiple degree of freedom equilibrium equations for the cantilever (29).

$$\begin{cases} \boldsymbol{M}\ddot{\boldsymbol{r}} + \boldsymbol{K}\boldsymbol{r} - \boldsymbol{\Theta} v = -\boldsymbol{B_f} \ddot{w}_B \\ \boldsymbol{\Theta}^{\mathbf{t}} \boldsymbol{r} + C_p v + q = 0 \end{cases} \quad (29)$$

Where $\boldsymbol{M}$, $\boldsymbol{K}$ are the equivalent mass and stiffness matrix, $\boldsymbol{\Theta}$, $\boldsymbol{B_f}$ the coupling and forcing vectors and C_p the piezoelectric material clamped capacitance. Their expressions for parallel electrical connection are given in equations (30) to (34).

$$\boldsymbol{K} = \left[\int_{\mathcal{V}_{p1}} \boldsymbol{\phi_r''}^t c_{11}^{ef} \left(z^2 + k_{e_{31}}^2 (z^2 - z_{m1}^2) \right) \boldsymbol{\phi_r''} \, dV_p + \int_{\mathcal{V}_{p2}} \boldsymbol{\phi_r''}^t c_{11}^{ef} \left(z^2 + k_{e_{31}}^2 (z^2 - z_{m2}^2) \right) \boldsymbol{\phi_r''} \, dV_p + \int_{\mathcal{V}_s} \boldsymbol{\phi_r''}^t Y_s^{ef} \, z^2 \boldsymbol{\phi_r''} \, dV_s \right] \quad (30)$$

$$\boldsymbol{M} = \int_0^{L_b} m \boldsymbol{\phi_r}^t \boldsymbol{\phi_r} dx + M_t \big(\boldsymbol{\phi_r}(L_b)\big)^t \boldsymbol{\phi_r}(L_b) + M_t D_t \big(\boldsymbol{\phi_r'}(L_b)\big)^t \boldsymbol{\phi_r}(L_b) + M_t D_t \big(\boldsymbol{\phi_r}(L_b)\big)^t \boldsymbol{\phi_r'}(L_b) + (I_t + M_t D_t^2) \big(\boldsymbol{\phi_r'}(L_b)\big)^t \boldsymbol{\phi_r'}(L_p) \quad (31)$$

$$\boldsymbol{\Theta} = B e_{31}^{ef} (h_p + h_s) \boldsymbol{\phi_r'}(L_b) \quad (32)$$

$$C_p = B \frac{2 L_b \epsilon_{33}^{ef}}{h_p} \quad (33)$$

$$\boldsymbol{B_f} = \int_0^{L_b} m\boldsymbol{\phi_r}^t dx + M_t\left(\boldsymbol{\phi_r}(L_b)\right)^t + D_t M_t\left(\boldsymbol{\phi_r'}(L_b)\right)^t \tag{34}$$

It is worth noting that $\boldsymbol{K}$ depends on $k_{e_{31}}^2$ which is a new relevant result compared to the expression proposed in [22] for which the electric field was supposed to be constant through the thickness of the piezoelectric layers. As $k_{e_{31}}^2$ is no longer negligible for strongly coupled materials, this new expression of the stiffness matrix allows better consideration of the electromechanical interactions.

2.4. Mode shapes determination

In order to evaluate equation (29), we determine the analytical expressions for the mode shapes $\phi_i(x)$ from a 2-DOF model assuming that the beam mass is negligible compared to the mass of the proof mass. Consequently, the bending moment M_y at any time and at each position of the neutral axis is related to the torque T and the force F applied by the proof mass at the end of the beam ($x = L_b$) and written as (35).

$$M_y(x,t) = T(t) + F(t)[L_b - x] \tag{35}$$

The bending stiffness YI and the moment M_y for a symmetric bimorph in short circuit condition are obtained from (27) and given in (36) and (37) [40]. By integrating equation (37) twice and considering the boundary conditions at the clamped end ($w(0,t) = 0$ and $w'(0,t) = 0$), we obtain the expression of the stiffness matrix K_{2DOF} given in (38). Where the rotation $\theta_{L_b}(t)$ is the slope $w'(L_b,t)$. The force and the torque due to the translation and rotation accelerations of the proof mass are expressed in (39) and (40) from [32].

$$YI = B\left[Y_s^{ef}\frac{h_s^3}{12} + c_{11}^{ef}\left(\frac{2}{3}\left(h_p + \frac{h_s}{2}\right)^3 - \frac{h_s^3}{12} + k_{e_{31}}^2\frac{h_p^3}{6}\right)\right] \tag{36}$$

$$M_y(x,t) = YI\frac{\partial^2 w(x,t)}{\partial x^2} \tag{37}$$

$$\begin{pmatrix} F \\ T \end{pmatrix} = [K_{2DOF}]\begin{pmatrix} w_{L_b} \\ \theta_{L_b} \end{pmatrix} = \frac{YI}{L_b^2}\begin{bmatrix} 12 & -6 \\ -6 & 4L_b \end{bmatrix}\begin{pmatrix} w_{L_b} \\ \theta_{L_b} \end{pmatrix} \tag{38}$$

$$F = YI\frac{\partial^3 w(L_b,t)}{\partial x^3} = M_t\ddot{w}_{L_b} + M_t D_t\ddot{\theta}_{L_b} \tag{39}$$

$$T = YI\frac{\partial^2 w(L_b,t)}{\partial x^2} = I_t\ddot{\theta}_{L_b} + M_t D_t^2\ddot{\theta}_{L_b} + D_t M_t\ddot{w}_{L_b} \tag{40}$$

Finally, equations (38) to (40) and the force and moment equilibrium analysis at the end of the beam lead to the 2-DOF coupled equation system (41) when no external excitation is considered.

$$\begin{bmatrix} M_t & M_t D_t \\ D_t M_t & I_t + D_t^2 M_t \end{bmatrix}\begin{pmatrix} \ddot{u}_{L_b} \\ \ddot{\theta}_{L_b} \end{pmatrix} + [K_{2DOF}]\begin{pmatrix} w_{L_b} \\ \theta_{L_b} \end{pmatrix} = \begin{bmatrix} 0 \\ 0 \end{bmatrix} \tag{41}$$

If we assume the deflection w_{L_b} and the rotation θ_{L_b} to be sinusoidal, defined by their angular frequency ω and their amplitudes W and O respectively, we can determine the first and second short circuit resonant frequencies of

the 2-DOF system (41) by solving (42). The resulting resonant frequencies (or pulsations) of the cantilever are expressed in appendix B.

$$\left(\omega^2 \begin{bmatrix} M_t & D_t M_t \\ D M_t & I_t + D_t^2 M_t \end{bmatrix} + \frac{YI}{L_p^2} \begin{bmatrix} \frac{12}{L_b} & -6 \\ -6 & 4L_b \end{bmatrix}\right) \begin{pmatrix} W \\ O \end{pmatrix} = \begin{bmatrix} 0 \\ 0 \end{bmatrix} \tag{42}$$

When applying the Rayleigh-Ritz method to the proposed 2-DOF model, the transverse displacement $w(x,t)$ is reduced to the sum of two bending modes ($i \in [1,2]$). From the resolution of (42), we determine the eigenvectors for each resonant frequency, $[W_1, O_1]$ and $[W_2, O_2]$, that we use to express the modes shapes $\phi_1(x)$ and $\phi_2(x)$.

According to equations (35) and (37), $\phi_1''(x)$ and $\phi_2''(x)$ are affine functions and can be expressed using two coefficients a_i and b_i as depicted in Figure 5 and equation (43). Therefore, as each mode shape satisfies the boundary conditions at the clamped end, only the eigenvectors values $[W_1, O_1]$ and $[W_2, O_2]$ are necessary to express the modes shapes, as $W_i = \phi_i(L_b)$ and $O_i = \phi_i'(L_b)$.

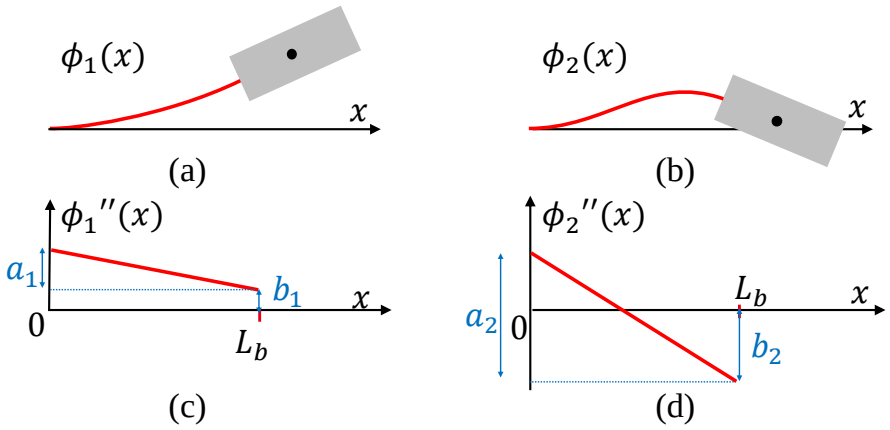

Figure 5: Representation of the mode shapes $\phi_i(x)$ and their second derivatives $\phi_i''(x)$ deduced from the 2-DOF model for the first two bending resonant frequencies.

$$\phi_i''(x) = b_i + a_i\left(1 - \frac{x}{L_b}\right) \tag{43}$$

$$\phi_i'(x) = \frac{x\left(2b_i - a_i\frac{x}{L_b} + 2a_i\right)}{2} \tag{44}$$

$$\phi_i(x) = \frac{x^2\left(3b_i - a_i\frac{x}{L_b} + 3a_i\right)}{6} \tag{45}$$

For the sake of simplicity, we define the rotation amplitude to deflection amplitude ratio $\beta_i = O_i/W_i$ that expresses the slope amplitudes at the end of the beam during bending for each mode. From equation (42), $\beta_1$and β_2 are expressed as:

$$\beta_1 = -\frac{3\,(2\,D_t + L_b)}{3\,J_t - (9\,D_t^4 + 18\,D_t^3 L_b + 15\,D_t^2 L_b^2 + 18\,D_t^2 J_t + 6\,D_t\,L_b^3 + 18\,D_t\,L_b\,J_t + L_b^4 + 3\,L_b^2 J_t + 9\,J_t^2)^{\frac{1}{2}} + 3\,D_t^2 - L_b^2} \tag{46}$$

$$\beta_2 = -\frac{3\,(2\,D_t + L_b)}{3\,J_t + (9\,D_t^4 + 18\,D_t^3 L_b + 15\,D_t^2 L_b^2 + 18\,D_t^2 J_t + 6\,D_t\,L_b^3 + 18\,D_t\,L_b\,J_t + L_b^4 + 3\,L_b^2 J_t + 9\,J_t^2)^{\frac{1}{2}} + 3\,D_t^2 - L_b^2} \tag{47}$$

With J_t termed the rotary inertia to mass ratio defined as $J_t = I_t/M_t$, the rotary inertia of the proof mass normalized by its mass, which only depends on the proof mass shape. For a rectangular proof mass, the values of J_t and D_t are given by $(L_m^2 + H_m^2)/12$ and $L_m/2$ respectively.

From equations (43) to (45), we express a_i and b_i as a function of W_i and O_i. Normalizing the modes shapes such as $W_i = 1$ and $O_i = \beta_i$, a_i and b_i are finally given in (48) and (49).

$$a_i = \frac{6\,(2 - L_b\beta_i)}{L_b^2} \qquad (48) \qquad\qquad b_i = \frac{2\,(2\,L_b\,\beta_i - 3)}{{L_b}^2} \qquad (49)$$

2.5. Rayleigh-Ritz method applied with the mode shapes

Once the mode shapes and their second derivatives are determined, we obtain the analytical expressions of the equivalent parameters of the system (29) by substituting them in (30) to (34). The coefficients of each matrix and vector are finally expressed in equations (50) to (53).

$$\begin{aligned} M_{ij} = {} & \frac{L_b^5 m\left(66\,a_i a_j + 91\,a_i b_j + 91\,a_j b_i + 126\,b_i b_j\right)}{2520} \\ & + \frac{L_b^2 (a_i + 2\,b_i)\left(a_j + 2\,b_j\right)(M_t D_t^2 + I_t)}{4} + \frac{L_b^4 M_t (2\,a_i + 3\,b_i)\left(2\,a_j + 3\,b_j\right)}{36} \\ & + \frac{D_t L_b^3 M_t (a_i + 2\,b_i)\left(2\,a_j + 3\,b_j\right)}{12} + \frac{D_t L_b^3 M_t \left(a_j + 2\,b_j\right)(2\,a_i + 3\,b_i)}{12} \end{aligned} \qquad (50)$$

$$K_{ij} = \frac{L_b\left(2\,a_i a_j + 3\,a_i b_j + 3\,a_j b_i + 6\,b_i b_j\right)}{6} YI \qquad (51)$$

$$B_{f_i} = \frac{L_b^2 M_t\,(3\,b_i + 2\,a_i)}{6} + \frac{L_b^3\,m(4\,b_i + 3\,a_i)}{24} + \frac{D_t\,L_b\,M_t\,(2\,b_i + a_i)}{2} \qquad (52)$$

$$\Theta_i = \frac{B\,L_b\,e_{31}^{ef}\,(2\,b_i + a_i)\left(h_p + h_s\right)}{2} \qquad (53)$$

As the first bending mode is the most coupled for this given structure [41], this paper focuses on the first resonant mode. We then approximate the behavior of the piezoelectric cantilever using its related model around the first resonant mode and we reduce the 2-DOF system to the SDOF system (1) (where $M = M_{11}$, $K = K_{11}$, $\Theta = \Theta_1$, $B_f = B_{f_1}$). However, the 2-DOF model could be useful to design a cantilever for which the second resonant frequency can be located at a chosen value (*e.g.* to avoid interaction between modes).

We eventually propose in (54) an analytical expression of k_e^2 the square of the alternative electromechanical coupling coefficient of a cantilever with a proof mass deduced from equations (4), (33), (52) and (53).

$$k_e^2 = k_{e_{31}}^2 \mathcal{R}_L \mathcal{R}_T \qquad (54)$$

$$\mathcal{R}_L = \frac{\left(\frac{b}{a}\right)^2 + \left(\frac{b}{a}\right) + \frac{1}{4}}{\left(\frac{b}{a}\right)^2 + \left(\frac{b}{a}\right) + \frac{1}{3}} \qquad (55)$$

$$\mathcal{R}_T = \frac{\left(\frac{h_p}{h_s}\right)^3 + 2\left(\frac{h_p}{h_s}\right)^2 + \left(\frac{h_p}{h_s}\right)}{\frac{1}{6}\left(\frac{Y_s^{ef}}{c_{11}^{ef}}\right) + \frac{4 + k_{e_{31}}^2}{3}\left(\frac{h_p}{h_s}\right)^3 + 2\left(\frac{h_p}{h_s}\right)^2 + \left(\frac{h_p}{h_s}\right)} \qquad (56)$$

$\mathcal{R}_L$ and $\mathcal{R}_T$ are two factors termed "length factor" and "thickness factor" respectively. $\mathcal{R}_L$ only depends on the strain distribution along the beam, as expressed in (55) while $\mathcal{R}_T$ is related to the stress distribution across the thickness of the beam (56).

As we only consider the first resonant frequency, in the following, the coefficients a and b represent a_1 and b_1. As the b/a ratio is related to the second derivative of the transverse deflection, it expresses the homogenization of the strain distribution along the beam (the higher b/a, the better the homogenization). The b/a ratio is expressed thanks to (46), (48) and (49) in (57).

$$\frac{b}{a} = -\frac{3J_t - (9\,D_t^4 + 18\,D_t^3 L_b + 15\,D_t^2 L_b^2 + 18\,D_t^2 J_t + 6\,D_t L_b^3 + 18\,D_t L_b J_t + L_b^4 + 3\,L_b^2 J_t + 9\,J_t^2)^{\frac{1}{2}} + 3\,D_t^2 + L_b^2 + 4\,D_t L_b}{6\,J_t - 2\,(9\,D_t^4 + 18\,D_t^3 L_b + 15\,D_t^2 L_b^2 + 18\,D_t^2 J_t + 6\,D_t L_b^3 + 18\,D_t L_b J_t + L_b^4 + 3\,L_b^2 J_t + 9\,J_t^2)^{\frac{1}{2}} + 6\,D_t^2 + L_b^2 + 6\,D_t L_b} \quad (57)$$

To our knowledge, for the first time, an analytical expression of the alternative electromechanical coupling coefficient is provided for a piezoelectric cantilever with a full proof mass geometry taken into account and when a variable electric field across the piezoelectric patches is considered. This expression is used in the next section to propose design guidelines.

3. Design guidelines for optimization

Because k_e^2 depends both on the material coupling coefficient and the structure geometry, they have to be taken into account simultaneously: i) by using strongly coupled materials (e.g. PZT ceramics or relaxor-based ferroelectric single crystals such as PMN-PT and PZN-PT), ii) by optimizing the devices to direct the stress in the piezoelectric material and to make its distribution as uniform as possible.

We have previously demonstrated that k_e^2 of our harvester can be optimized by maximizing the length factor $\mathcal{R}_L$ (§3.1), the thickness factor $\mathcal{R}_T$ (§3.2) and the squared material expedient electromechanical coupling coefficient $k_{e_{31}}^2$ (§3.3). As k_e^2 cannot be higher than $k_{e_{31}}^2$, both $\mathcal{R}_L$ and $\mathcal{R}_T$ are lower than one and the purpose of the optimization process is to keep them as close to unity as possible. The optimization of the longitudinal stress distribution and the transverse stress distribution (*i.e.* optimization of $\mathcal{R}_L$ and $\mathcal{R}_T$) can be done separately as they do not depend on the same parameters. We discuss hereafter how these factors can be maximized.

3.1. Optimization of $\mathcal{R}_L$

From equation (55) in section 2, Figure 6 plots the evolution of $\mathcal{R}_L$ as a function of the b/a ratio.

$\mathcal{R}_L$ tends toward one as b/a tends toward infinity. It can also be seen that $\mathcal{R}_L$ = 0.75 when b/a = 0 (i.e. for the case of a cantilever with a point proof mass placed at the end of the beam ($J_t = 0$ and $D_t = 0$)). As a conclusion, the optimal configuration of the longitudinal strain distribution would lead to an increase of k_e^2 by 33% compared to the point mass case. It can also be noted that even a moderate b/a ratio allows to achieve high values of $\mathcal{R}_L$ (*e.g.* $\mathcal{R}_L$ = 0.964 for b/a = 1).

Equation (57) shows that b/a depends on the proof mass geometric characteristics (J_t and D_t) and the beam length L_b. Figure 7 plots $\mathcal{R}_L$ as a function of J_t and D_t for a constant beam length. It highlights the interest of increasing both J_t and D_t. Even if $\mathcal{R}_L$ is theoretically maximal for a null value of D_t when J_t is very large (not perceptible on the figure), it is more convenient to design devices with a moderate to large value of J_t and a moderate to large value of D_t.

Designs that involve a large J_t and a low D_t lead to harvesters with too large overall volumes that they would be difficult to fabricate. For instance, a height to length ratio of a rectangular proof mass H_m/L_m = 7 is necessary to reach $\mathcal{R}_L$= 0.943 with J_t = 150mm² and D_t = 3 mm (L_b = 20 mm, L_m = 6 mm, H_m= 42 mm) while a long and thin proof mass (e.g H_m/L_m = 0.4) reaches roughly the same $\mathcal{R}_L$ (0.949) (L_b = 20 mm, L_m = 25 mm, H_m =10mm). These examples show that increasing the proof mass length L_m is a simple and efficient solution to optimize $\mathcal{R}_L$ since it both increases J_t and D_t while reducing the overall volume of the harvester. It is also interesting to note that only the beam length and the proof mass's shape modify b/a and $\mathcal{R}_L$ whatever the material densities.

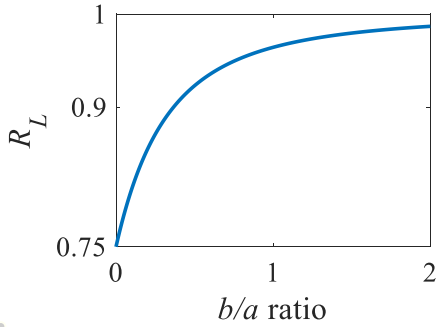

Figure 6: $\mathcal{R}_L$ as a function of b/a. b/a is positive for the first resonant mode for $D_t \geq 0$.

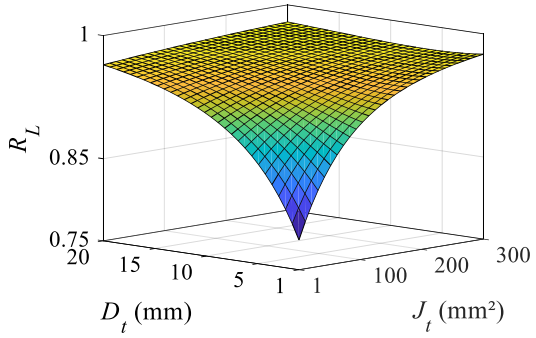

Figure 7: Evolution of $\mathcal{R}_L$ factor with the distance D_t and rotary inertia to mass ratio J_t for a beam length L_b of 20mm.

3.2. Optimization of $\mathcal{R}_T$

As depicted in Figure 8, $\mathcal{R}_T$ is maximal for an optimal thickness ratio $\left(h_p/h_s\right)^{opt}$. This optimal ratio (58) only depends on the κ ratio as defined in (59).

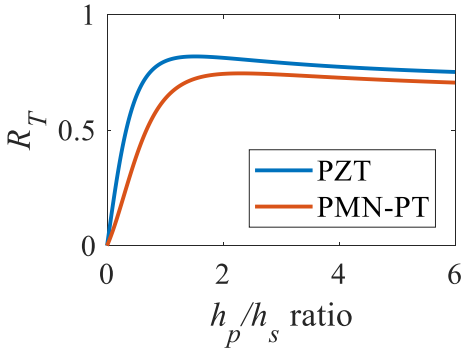

Figure 8: $\mathcal{R}_T$ as a function of the thickness ratio for PZT or PMN-PT patches and steel substrate ($Y_s =$ 200 GPa). Plane stress assumption and piezoelectric coefficients of Table 1 are considered.

$$\left(\frac{h_p}{h_s}\right)^{opt} = \begin{cases} \frac{1}{2}\kappa^{\frac{1}{3}}\left[\left(1-\sqrt{1-\kappa}\right)^{\frac{1}{3}}+\left(1+\sqrt{1-\kappa}\right)^{\frac{1}{3}}\right] & \text{for } \kappa \leq 1 \\ \sqrt{\kappa}\cos\left(\frac{\arctan\sqrt{\kappa-1}}{3}\right) & \text{for } \kappa > 1 \end{cases} \tag{58}$$

$$\kappa = \frac{Y_s^{ef}}{c_{11}^{ef}}\frac{1}{k_{e_{31}}^2+1} \tag{59}$$

As the longitudinal strain increases linearly with the distance from the neutral axis (Euler-Bernoulli assumption), one might think that the configuration with thin patches located far away from the neutral axis (*i.e.* low h_p/h_s) is the best one. Nevertheless, this configuration also means that a lot more elastic energy is stored in the substrate than in the piezoelectric material. Thus, the optimal ratio $\left(h_p/h_s\right)^{opt}$ matches a trade-off between maximizing the elastic energy in the piezoelectric material and homogenizing the strain distribution.

It is interesting to notice that κ not only depends on the piezoelectric stiffness c_{11}^{ef} but also on the square of the material expedient coupling coefficient k_{e31}^2 as we considered a variable electric field across the patches' thicknesses. This is a significant improvement compared to former works on global coupling optimization [18,42], since strongly coupled materials (*e.g.* PZN-PT or PZT) are used to improve the coupling coefficient of the global system.

By using (58) and (59), the maximal value of $\mathcal{R}_t$ can be determined for given materials and is limited by κ and $k_{e_{31}}^2$. As an example, for PMN-PT and PZT materials in plane stress configuration associated to steel substrate, the optimal thicknesses ratio are 2.3 and 1.5 respectively and the maximal values of $\mathcal{R}_t$ are 0.74 and 0.82 respectively. In comparison, the maximal value of $\mathcal{R}_t$ as well as its optimum are different in plane strain configuration: $\mathcal{R}_t$ = 0.65 and 0.81 at $\left(h_p/h_s\right)^{opt}$ = 1.6 and 1.4 for the PMN-PT and PZT respectively.

Finally, as $\mathcal{R}_T$ and $\mathcal{R}_L$ do not depend on the total thickness of the beam nor on the material density of the proof mass, we can adjust them for the sole purpose of targeting to a desired frequency without hindering the coefficient k^2. This result established from the proposed model simplifies the design of vibration harvesters for coupling optimization.

3.3. Optimization of $k_{e_{31}}^2$

In addition to the optimization of the $\mathcal{R}_T$ and $\mathcal{R}_L$ factors, we can increase k_e^2 by maximizing the piezoelectric material coupling coefficient. This can be done through the use of strongly coupled materials and by the optimization of the aspect ratio of the beam (width-to-length ratio B/L_b). Indeed, the effective electromechanical coupling coefficient of piezoelectric materials shows a considerable difference between the plane stress and plane strain assumptions (Table 1). Some materials, such as PZT ceramics and [001] poled PMN-PT single crystals, present a larger coupling coefficient in the plane strain configuration, while other ones (*e.g.* [011] poled PZN-PT) exhibit larger coupling coefficient in plane stress configuration [43]. These inclinations depend on the crystal classes, the poling directions and the cut orientations. Therefore, we should design wide beams for the first category and narrow beams for the second one.

Due to their symmetry, the PZT ceramics exhibit larger material coupling coefficients for wide beams than for narrow ones. However, wide systems could become an issue if small volume devices or low resonant frequencies are required. The sought B/L_b ratio is often higher than 5 in order to satisfy the plane strain assumption [37] and the length of the beam would be chosen as long as possible to lower the resonant frequency. Therefore, a tradeoff has to be found regarding to the width-to-length ratio of the device.

Table 1: Properties of the piezoelectric materials chosen for the study
(the material coupling coefficients expressions are extracted from [44]).

	d_{31} (pm.V^{-1})	s_{11}^E (×10^{-12}Pa^{-1})	ϵ_{33}^T (F.m^{-1})	$k_{31}^{l\,2}$ plane stress	$k_{31}^{w\,2}$ plane strain	Curie Temperature (°C)	ρ_p (kg.m^{-3})
TRS X2B [001] PMN-29PT [45]	-699	52.1	5400 ϵ_0	19.6%	68.1%	170	7750
Noliac NCE51 PZT-5A [46]	-208	17	1900 ϵ_0	15.1%	34.3%	360	7850

3.4. Optimal designs proposals

To validate the design guidelines, we hereafter propose three strongly coupled piezoelectric cantilevers involving two types of piezoelectric material: PMN-PT single crystal and PZT-5A ceramic. A targeted resonant frequency of 30Hz has been chosen as many applications for vibration harvesting are low frequency applications. The two first prototypes (one PMN-PT based and one PZT based) are designed with low width-to-length ratio corresponding to the plane stress assumption.

The maximal theoretical power that can be harvested by a piezoelectric cantilever is given by the SDOF model (1) and is expressed as (60) for a sufficiently coupled device with moderate mechanical losses ($k_e^2 Q_m > 2$).

$$P_{max} = \frac{B_f^2}{M}\frac{Q_m}{8\omega_1}|\ddot{w}_b|^2 \tag{60}$$

We design the two first generators to present the same resonant frequency and the same coefficient B_f^2/M so that the mechanical quality factor is the only remaining parameter that affects the maximal generated power at a given acceleration.

We choose a rectangular shape for the proof mass to facilitate the fabrication process. Steel ($Y_s = 200$ Gpa, $\nu = 0.3$ and $\rho_s = 7930$ kg. m^{-3}) is chosen as the substrate and the proof mass material as it presents low intrinsic mechanical losses and a large value of yield strength.

The optimal designs have been obtained using the proposed model with some constraints since suppliers limit the accessible thicknesses of piezoelectric and steel plates. The obtained final designs for PMN-PT N and PZT N are detailed in Table 2. The adjustments on the thicknesses have an impact on the theoretical global electromechanical coupling coefficients but strong coupling coefficients are still expected. With the optimal configuration, the theoretical k^2 are expected to reach 15.2% and 12.8% for the PMN-PT N and PZT N respectively. Due to the aforementioned adjustments with the final dimensions, they are expected to be equal to 12.9% and 11.8% respectively. The two optimal structures implement a long proof mass to homogenize the longitudinal strain distribution.

As the material coupling coefficient $k_{31}^2$of PZT is lower than the one of PMN-PT, a same trend is expected for k^2. Thinner or/and longer piezoelectric layers are also necessary to reach the same resonant frequency as the stiffness of the PZT ceramic is larger than the one of the PMN-PT single crystal. PMN-PT represents a convenient material when low frequency and strong global coupling coefficient are expected. Nevertheless, the PZT-5A material may be advantageous as it is much cheaper and best suited for higher temperature applications.

Table 2: Geometrical parameters of the three proposed prototypes
(N holds for the 2 narrow prototypes and W for the widest prototype)

Design name	**"PMN-PT N"**	**"PZT N"**	**"PZT W"**
Material	PMN-PT	PZT-5A	PZT-5A
Beam length L_b	45 mm	15 mm	15 mm
Mass length L_m	45 mm	60 mm	60 mm
Height of mass H_m	5 mm	10 mm	10 mm
Beam and mass width B	10 mm	5 mm	25 mm
Substrate thickness h_s	0.5 mm	0.4mm	0.4mm
Piezoelectric thickness h_p	0.5 mm	0.3 mm	0.3 mm
Width-to-length ratio B/L_b	0.22	0.33	1.67
Coefficient B_f^2/M	18.2 g	19.8 g	99.1 g

In order to study the width B influence on k^2 and to design a PZT-based device with a strong global coupling coefficient, we also built a third prototype (PZT-W) with same parameters as the PZT-N device (Table 2) while widening the beam. However, we selected a moderate value of width to limit the volume of the harvester. The beam width equals 25mm (5 times larger than the PZT-N design). The dimensions of the PZT-W design are listed in Table 2.

4. Experimental validations

4.1. Prototypes fabrication and impedance measurements

The PMN-PT patches from TRS technologies and PZT patches from Noliac have been cut to size by the manufacturers and glued in our laboratory on steel beams with non-conductive epoxy glue (Epotecny E505). During the gluing process, a strong compressive force is applied to electrically connect the middle electrode of the piezoelectric patches to the conductive substrate (steel beam) making the glue thickness *a priori* negligible. The proof mass is made from two steel sheets bonded on the substrates with a 3M® epoxy glue. The clamped end is obtained by screwing steel thick parallelepipeds to sandwich the other end of the substrate beam (Figure 9). Figure 10 shows the three assembled prototypes.

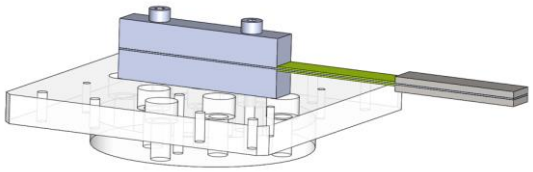

Figure 9: 3D CAD design of the PMN-PT N device and its interface for shaker.

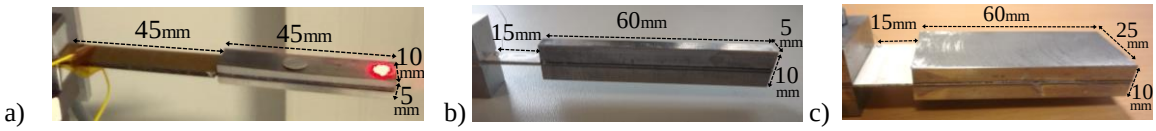

Figure 10: Pictures of the assembled prototypes showing a) the PMN-PT N design, b) the PZT N design and c) the PZT W design.

Impedance measurements have been performed on each prototype (Figure 11) with a 6500B series impedance analyze from Wayne Kerr®. The short circuit resonant frequencies f_{sc} and the squared global electromechanical coupling coefficients k^2 are determined with the method presented in [33] and are compared to the ones determined with the proposed model, 2D FEM simulations and 3D FEM simulations. The results are presented in Table 3. In the case of FEM simulations, the k^2 are obtained by performing $(f_{sc}^2 - f_{oc}^2)/f_{oc}^2$ where f_{sc} and f_{oc} are the computed the short circuit and open circuit resonant frequencies, respectively. 2D-FEM and proposed model were used according to the plane stress assumption for PMN-PT N and PZT N designs and the plane strain assumption for the PZT W design.

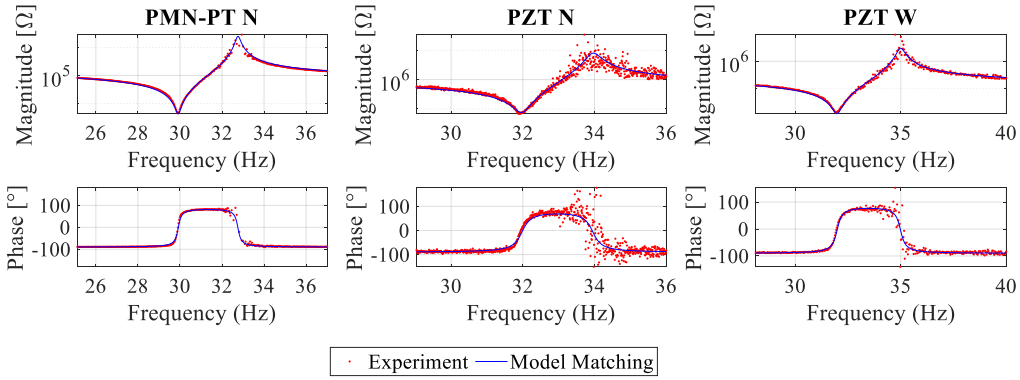

Figure 11: Magnitude and phase of the measured impedance on each prototype and model curves with the fitted parameters.

Table 3: Short circuit resonant frequency f_{sc} and squared global electromechanical coupling coefficient k^2 of the three prototypes deduced from modeling, simulations and impedance measurements

		Design PMN-PT N	**Design PZT N**	**Design PZT W**
Proposed Modeling	f_{sc}	31.2Hz	34.2Hz	36.3Hz
	k^2	12.9%	11.8%	27.9%
2D-FEM	f_{sc}	31.2Hz	34.1Hz	36.2Hz
	k^2	12.6%	11.5%	27.3%
3D-FEM	f_{sc}	34.3 Hz	34.8 Hz	35.8 Hz
	k^2	21.3%	14.2%	23.3%
Impedance Measurement	f_{sc}	29.9 Hz	32.0 Hz	32.0 Hz
	k^2	16.6 %	11.3%	16.4%

4.2. Comparison between analytical model, FEM simulations and experiments results

From Table 3, we can notice a very good agreement between the model and 2D-FEM simulations. However, these results do not match perfectly with the 3D-FEM ones. Indeed, the width-to-length ratios of designed structures (Table 2) favor either the plane stress assumption or the plane strain assumption, which are, nevertheless, only a simplification for analytical modeling and 2D-FEM approaches. For designs with intermediate width-to-length ratios (from 0.2 to 5), models that explicitly consider the width-to-length ratio appear therefore interesting [47]. However, they do not take the width-to-thickness ratio into account while it has been shown to be also involved in the out-of-plane stress interaction [48]. As a solution, 3D-FEM simulations can be used to analyze the stress distribution in the beams (Figure 12 and Figure 13) and to evaluate the influence of the beam width on k^2 (Figure 14).

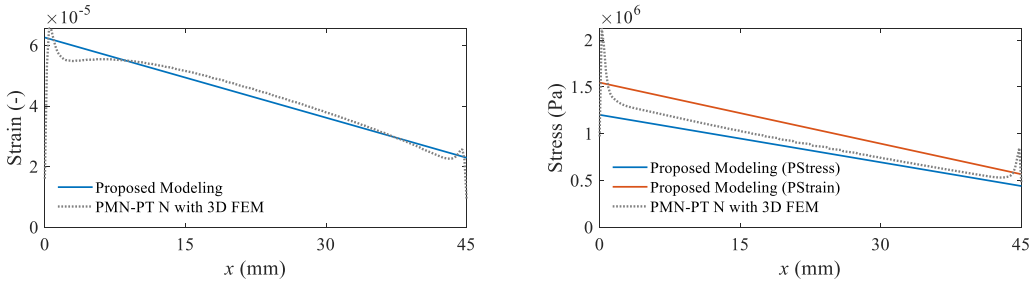

Figure 12: Strain and stress distributions along the center position of the upper piezoelectric patch ($z = z_{m2}$) of the PMN-PT N design for a displacement at $x = L_b$ equal to 0.1mm. PStress: plane stress, PStrain: plane strain.

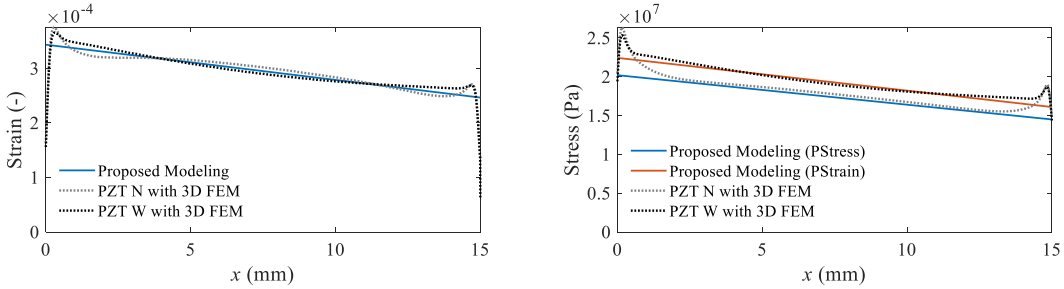

Figure 13: Strain and stress distributions along the center position of the upper piezoelectric patch ($z = z_{m2}$) of the PZT based designs for a displacement at $x = L_b$ equal to 0.1mm.

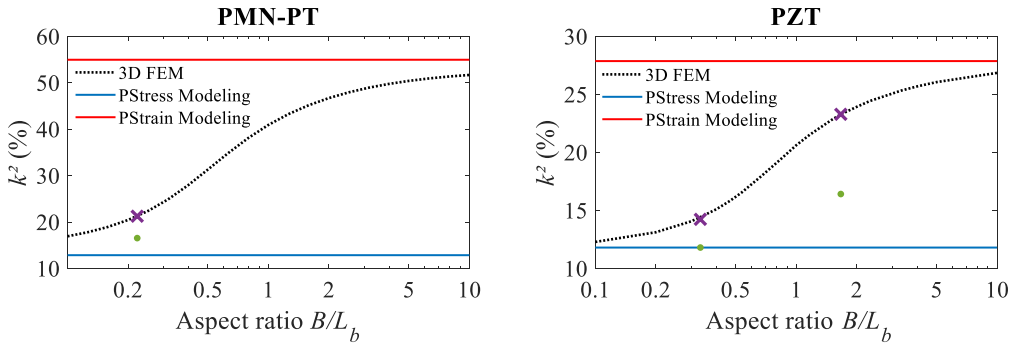

Figure 14: 3D simulated coupling evolution as a function of the beam width for the PMN PT and PZT devices. The other geometrical parameter are in Table 2. The crosses and the dots stand for the simulated and the experimental results respectively of the designed prototypes.

The model appears to determine accurately the strain and stress compared to the 3D-FEM simulations and just a slight difference is noticed between the plane stress modeling and the 3D-FEM results for the PMN-PT N design. Furthermore, for small and large width-to-length ratios (*i.e.* B/L_b equal to 0.1 and 10 respectively), k^2 is

accurately determined for designs using PZT material while there still is a difference for designs using PMN PT. These differences are thought to be due to the out-of-plane interactions associated to a strong material coupling coefficient as approximations of the effective piezoelectric material parameters are done in the model.

Despite the consideration of the beam width-to-length ratio, lower $k^2$are measured on the prototypes than the ones expected by the 3D-FEM simulations (Table 2), which could be explained by the clamping configuration and the glue thickness. Due to prototypes' configuration, functional clearances between the patches and the stationary frame at one end and between the patches and the proof mass on the opposite end are required. Even if these distances and the glue thickness cannot be accurately determined and are limited, they induce a drastic decrease of k^2. As an example, the squared global coupling coefficient k^2 of the PZT W design is equal to 17.0% if we consider the clearances equal to 1 µm and a glue thickness of 5 µm in a 3D-FEM simulation (for which the epoxy glue Young's modulus is assumed to be 4 GPa) compared to 23.3% in the case of perfect clamping and bonding.

The proposed model approximates the k^2 of the final prototypes due to assumptions on the effective material parameters and manufacturing variations not considered. Yet, the model is relevant to study the strain and the stress distributions and provides critical information for a design optimization as it brings to light the underlying physical explanations.

4.3. Discussion on experimental global coupling coefficients measurements

From the impedance measurements, the global coupling coefficients k^2, the quality factors Q_m and the figure of merit $k_e^2 Q_m$ of the prototypes are reported in Table 4 as well as comparisons to the values from the state of the art . We also propose a new figure of merit: the Structural Coupling Optimization $SCO = k^2/\max(k_{31}^{l\,2}; k_{31}^{w\,2})$ defined as the global coupling coefficient normalized by the maximal coupling coefficient of the material between the plane stress and the plane strain assumptions. It indicates the ability of the proposed structure to takes benefit of the material performance.

To our knowledge, the coefficients k^2 reached by our prototypes are the best experienced with PMN-PT [001] and PZT-5A based cantilevers compared to the state of the art. According to Table 4, devices made with relaxor-based ferroelectric single crystals show better coupling thanks to their strong material coupling coefficients. Some of these devices reach strong SCO values as their effective material coupling coefficients are maximal with narrow beams. In general, lower k^2 are reached with ceramics but our method allowed us to design the strongly coupled PZT W device that competes with the PMN-PT N design. Enlarging the beam width between the PZT N and PZT W devices, we succeed in increasing k^2 by +45%. To conclude on Table 4, we notice that the systems that exhibit the best structural coupling optimization are the devices that include a long proof mass. This validates that this shape improves the strain distribution and by doing so, maximizes the global electromechanical coupling.

Table 4: Performance comparison of the proposed prototypes with reported values from the state-of-the-art regarding the global coupling coefficient and the mechanical quality factor

	Reference	Material	Material coupling $k_{31}^{l\,2}$-$k_{31}^{w\,2}$	Quality factor Q_m	Global coupling k^2	$k_e^2 Q_m$	$SCO = \frac{k^2}{\max\left(k_{31}^{l\,2}; k_{31}^{w\,2}\right)}$	Characteristic
Single crystal based prototypes	[21]	PZN-PT	85% - N/A	28	53.0%	32	64%	▬
	[19,20]	PZN-PT	85%* - N/A	20•	49.9%	20	59%*	►
	[49]	PZN-PT	85% - N/A	50	15.4%	9.1	19%	►
	[50]	PMN-PT	N/A - N/A	22•	6.0%•	1.4	N/A	‖‖‖
	PMN-PT N	PMN-PT	20% - 68%	130	16.6%	26	24%	▬
Ceramic based prototypes	[51]	PZT-5H	19% - 46%	65	12.3%	9.1	27%	▲
	[22]	PZT-5A	12% - 27%	32	12.5%	4.6	46%	▬
	PZT N	PZT-5A	15% - 34%	85	11.3%	11	33%	▬
	PZT W	PZT-5A	15% - 34%	91	16.4%	18	48%	▬

▬ : Long proof mass, ►: Thickness tapered beam, ▲ : Width tapered beam ‖‖‖: Interdigitated electrodes
•: values deduced from figures, *: 33-piezoelectric mode is used.

4.4. Power measurements and discussions

Each prototype has been tested under vibration excitation to determine the output power and the frequency bandwidth for various accelerations levels. The experimental setup scheme, presented in Figure 15, consists in an electromagnetic shaker (K2075E-HT) driven by a DSpace board through a feedback integrating an accelerometer (PCB Piezotronics 356A17). The DSpace board is controlled by a dedicated Matlab script that defines the acceleration level and frequency and controls the programmable electrical resistances. The experiments have been done for 60 resistive loads between 1 kΩ and 2 MΩ over 100 excitation frequencies.

In order to compare the harvesters, we use the normalized power density NPD figure of merit (59) proposed in [52] where V is the volume.

$$NPD = \frac{P_{RMS}}{|\ddot{w}_b|^2 V} \tag{61}$$

As the volume is hardly available from the state-of-the-art, the device volume corresponds to the volume of the smaller rectangular block that can contain the device. The NPDs of each prototype on optimal resistive loads are plotted as a function of the frequency for several accelerations in Figure 16. The resulting bandwidths as defined in section 2.1 and the maximal NPDs are plotted as a function of the acceleration level in Figure 17.

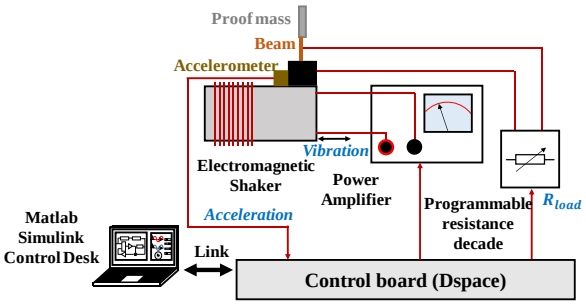

Figure 15: Representation of the experimental setup used for vibration testing

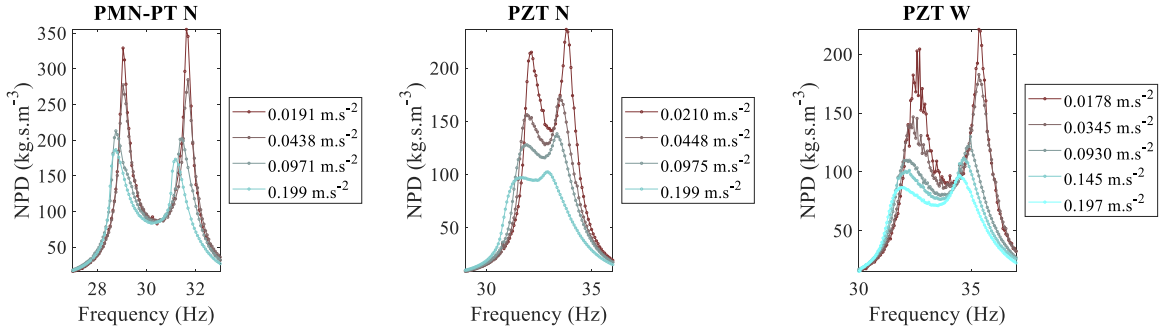

Figure 16: Normalized power densities measured for the three prototypes, for various excitation accelerations

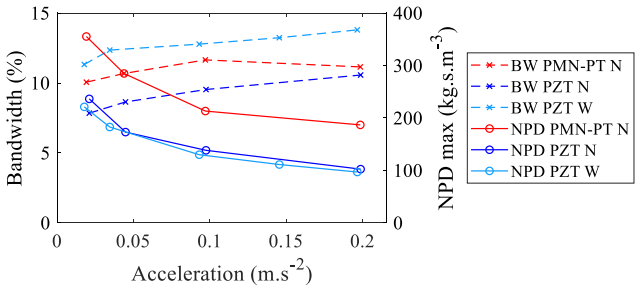

Figure 17: Frequency bandwidth and maximal NPD of the three prototypes as a function of the excitation acceleration

Our prototypes exhibit a nonlinear (softening) behavior when the excitation acceleration increases (Figure 16 and Figure 17). The maximal NPD values are approximately divided by 2 for each prototype when the acceleration

level is multiplied by 10 (from 0.02 $m.s^{-2}$ and 0.2 $m.s^{-2}$), while the bandwidth is increased by 11%, 34% and 22% for the PMN-PT N, PZT N and PZT W devices respectively. Large stress occurs in the piezoelectric patches even at low acceleration due to the combination of the low resonant frequency and large proof masses, which induces large displacement amplitudes at the end of the beam. However, the analysis of non-linear effects on our prototypes is out of the scope of this paper. Besides, other works have thoroughly studied the nonlinear behavior of piezoelectric cantilevers [53].

Table 5 reports the maximal value of the NPDs of our harvesters and for the state of the art. Two volumes are considered for normalization: the piezoelectric and the global volumes. While normalizing by the global volume appears interesting in order to consider constraints in terms of available space, normalizing by the volume of piezoelectric material will underline the structures that best optimize the use of the piezoelectric material, for cost reduction as an example. We also report the bandwidth when available. Table 5 is limited to strongly coupled harvesters. Additional devices exhibiting significant NPDs but limited bandwidths can be found in other works [54,55].

Our harvesters' maximal NPDs are among the best of the reported values. In general, devices that integrate a long proof mass appear to have large NPD values. The long proof mass reduces the resonant frequency while optimizing the global volume. Then, large normalized output power is reached, as the power is inversely proportional to the frequency (for a given ambient acceleration level). Moreover, we take full advantage of the piezoelectric material thanks to a long proof mass: the longitudinal strain in the piezoelectric layers is almost uniform and the value of the coefficient B_f^2/M in equation (60) is large compared to the piezoelectric volume. The PZT N device exhibits larger losses than the PMN-PT N device as it generates lower power while having almost the same value of B_f^2/M.

However, the long proof mass configuration tends to increase the deflections at the tip end of the proof mass and may not be the optimal design to increase the NPD if we consider the overall swept volume. Nevertheless, even in this case, our NPDs compete with the bests of the state-of-the-art. Considering the maximum tip displacements, the NPDs including the swept volumes are indeed equal to 298 $kg.s.m^{-3}$, 227 $kg.s.m^{-3}$ and 214 $kg.s.m^{-3}$ for the PMN-PT N, PZT N and PZT W respectively at the accelerations reported in Table 5.

Our prototypes present a large frequency bandwidth. Even if the frequency bandwidth of the PZT N device is remarkable for a cantilever (7.8%), the one of the PMN-PT N is larger (10.1%) due to its higher global coupling coefficient. Furthermore, thanks to the width increase, the PZT W prototype considerably enhances the bandwidth (11.3%) compared to the PZT N while keeping almost the same NPD (Table 5). At an acceleration of 0.2 $m.s^{-2}$, the prototypes PMN-PT N, PZT N and PZT W generate 33.1 µW, 15.1 µW and 70.3 µW respectively.

Table 5: Performances of the fabricated prototypes and comparison to the state-of-the-art in terms of normalized power density and bandwidth

	Reference	Active volume (mm^3)	Piezoelectric volume (mm^3)	Frequency (Hz)	Acceleration amplitude ($m.s^{-2}$)	Maximal Power RMS (µW)	NPD on total volume ($kg.s.m^{-3}$)	NPD on piezoelectric volume ($\times 10^3.kg.s.m^{-3}$)	Bandwidth
Single crystal based prototypes	[21]	1000	350	48.5	0.707	47.1	94.3	1.89	39.0%[a]
	[19,20]	6750	50	208	0.981	480	73.9	1.43	32.7%
	[49]	N/A	N/A	253	5.69	670	N/A	N/A	7.5%•
	[50]	1.21	0.148	406	14.7	7.18	27.2	0.224	N/A
	PMN-PT N	4500	450	29.1	0.0191	0.586	355	3.55	10.1%
Ceramic based prototypes	[51]	3750	104	116	2.45	88.8	3.94	0.142	N/A
	[22]	12300	926	41.6	0.500	160	52.2	0.691	N/A
	PZT N	3750	45	32.1	0.0210	0.393	236	19.7	7.8%
	PZT W	18750	225	32.5	0.0178	1.31	221	18.4	11.3%

• values deduced from figures, [a] estimated from theory

4.5. Operation with a dedicated integrated circuit

In this section, we demonstrate that the input/ambient vibration frequency can be dynamically tracked thanks to a strongly coupled harvester leveraged by an integrated circuit (Figure 18) developed in our group [12].

In several real-world applications, the host structure of the harvester has a vibration spectrum with a dominant frequency that fluctuates [5]. As an example, Beeby *et al.* [56] showed that the dominant vibration frequencies of a water pump in a combined heat and power plant fluctuates in the range of 210 Hz to 219 Hz (5%) due to variations of the pump speed. The vibrations of a ferry vehicle engine reported in [56] have a dominant frequency that varies from 48 Hz to 50 Hz (4%). Furthermore, temperature variations and/or aging of the harvester may alter the resonant frequency of the harvester. For instance, both Wozniak *et al.* [57] and Gasnier *et al.* [8] measured drifts in the resonant frequencies of their harvesters dedicated to aeronautic environment when subjected to temperature variations. Wozniak *et al.* measured a shift in the resonant frequency of their PMN-PT harvester of -7.0% between 0°C and 70°C while Gasnier *et al.* measured a shift of -5.6% with a PZT-5A harvester between 90°C and 120°C. Concerning the aging effects, Hoang *et al.* [6] measured a decrease of around 6% of the resonant frequency of their piezoelectric cantilevers after 6.7 billon cycles. Furthermore, a drift of 1% of the resonant frequency of the harvester of Benchemoul *et al.* [58] dedicated to HVAC systems led to a decrease of 30% of the harvested power compared to a frequency adjusted case. In order to harvest vibration energy from the above-mentioned environments, a harvester with a frequency bandwidth of at least 10% seems unavoidable to solve the problems of frequency shifts.

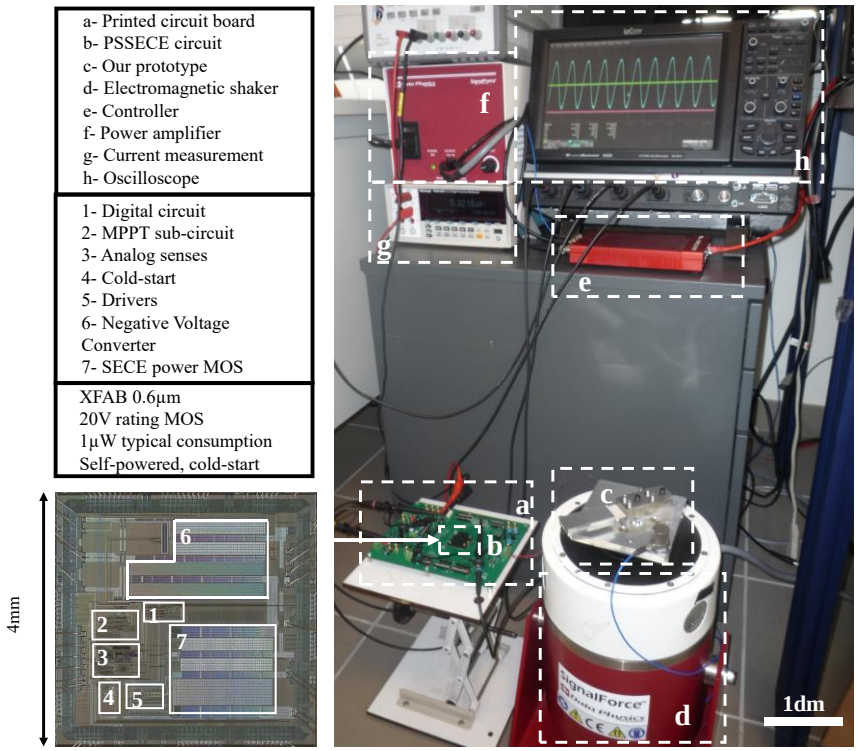

Figure 18: Experimental setup used to validate the high tunability of our highly coupled prototype connected to our self-adjustable self-powered harvesting circuit.

In order to lie within the range of reported HVAC vents vibration frequencies [58,59], we designed a new prototype with a short-circuit resonant frequency of 52,5 Hz. The new prototype shares the same dimensions with the PZT W devices depicted in Table 2, while the proof mass is made of aluminum instead of steel. The squared global electromechanical coupling coefficient k^2 of the prototype is 16.8%. On another note, this experimentally confirms that the material of the proof mass does not have much influence on the global coupling coefficient, since this new prototype exhibits almost the same coupling as the PZT W device (Table 4). Our highly coupled prototype has been tested along with an integrated circuit, presented in [12], which realizes the Phase-Shift SECE (PSSECE) harvesting technique [35].

The SECE strategy has initially been developed by Lefeuvre *et al.* [60] in 2005. During most of the vibration semi-periods, the harvester works in open-circuit condition. The absolute value of the voltage across the piezoelectric patches grows as electrical charges accumulate in the piezoelectric capacitance. As soon as the voltage reaches an extremum, an inductor is connected to the piezoelectric patches. The piezoelectric voltage quickly drops to zero as and the energy is quickly transferred to the inductor to be finally conveyed toward a storage capacitor. The Phase-Shift SECE, also introduced by Lefeuvre *et al.* in 2017 [35], is a harvesting technique derived from the SECE. In the PSSECE sequencing, the energy is extracted from the piezoelectric material with a tunable phase-shift comparatively with the standard SECE. The value of this phase-shift, thanks to the important backward coupling of our prototype, substantially influences the harvester dynamics, and allows a fine tuning of its resonant frequency on a relatively large frequency band.

The circuit incorporates a high-voltage power management stage, a cold-start, and a maximal power point tracking (MPPT) sub-system. The circuit is assembled onto a printed circuit board (PCB) and connected to the strongly coupled harvester. The experimental setup is shown in Figure 18. The signal generator sends an alternative signal to a power amplifier, which actuates the electromagnetic shaker. The PZT prototype fixed on the shaker is subjected to a sinusoidal excitation at frequencies ranging from 46 Hz to 65 Hz and having an amplitude of 0.98 m/s² (corresponding to the acceleration level indicated in [58]). The prototype is connected to the PSSECE circuit, which transmits the extracted power in an off-chip storage capacitor of 94µF.

Figure 19 shows the transient waveforms of the measured voltages obtained with the PSSECE circuit at the excitation frequency of 58 Hz and after a frequency shift to 53 Hz. During the first 4 seconds, the circuit gathers energy in the storage capacitor in a non-optimal way, in order to cold-start. Thereafter, when the voltage across the capacitor reaches 1.9V (meaning that the circuit has collected enough energy to start its optimal operation), the SECE techniques starts. The MPPT sub-system starts adjusting the phase-shift of the harvesting events, which consequently tunes the prototype resonant frequency. From the 5th to 17th second, the voltage magnitude keeps increasing, meaning that the harvested power increases. The extracted power is almost maximal and greater than 200 µW only 19 seconds after starting the circuit. Around the 19th second, we manually change the vibration frequency from 58 Hz to 53 Hz, leading to a quick drop of the voltage across the harvester. Immediately, the MPPT sub-system automatically starts converging to a new optimal phase-shift in order to bring the prototype resonant frequency closer to the new vibration frequency. Once again, the good convergence of the MPPT sub-system is illustrated by an increase of the voltage magnitude, until the 33th second. Through this experiment, we show that the system generates an optimal useful power even shortly after large frequency variations.

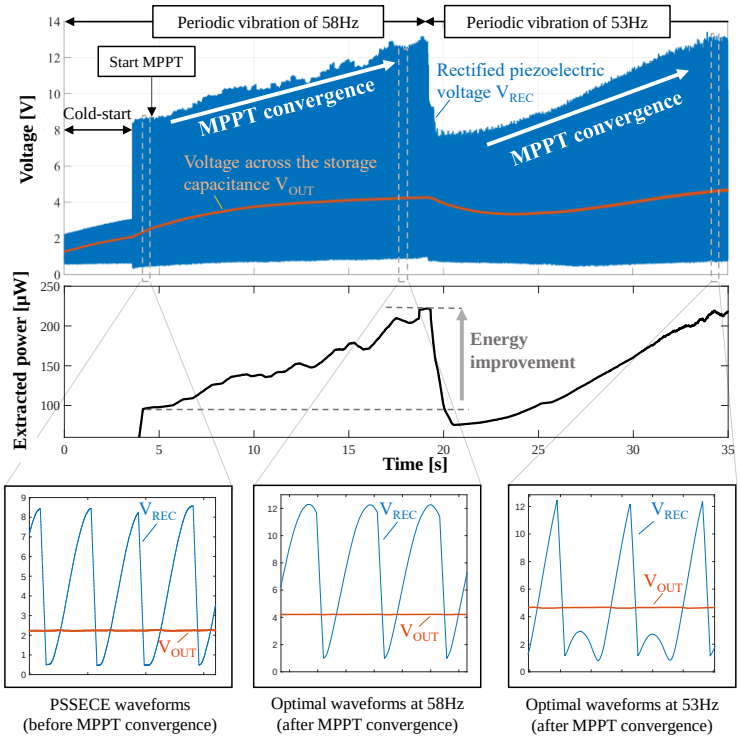

Figure 19: Transient response of our prototype connected to the PSSECE circuit illustrating the resonant frequency self-adjustment when the vibration frequency shifts from 58 Hz to 53 Hz.

Figure 20 shows the power-frequency response measured with our prototype connected to the PSSECE circuit. The harvested power was measured by multiplying the average current flowing into the storage capacitor with the DC voltage across it after convergence of the MPPT sub-system for 20 vibration frequencies equally spaced between 46 Hz and 65 Hz. The results shown in Figure 20 demonstrate that our system is able to harvest more than 100 µW for vibration frequencies ranging from 50 Hz to 62 Hz. This represents enough power to supply a wireless sensor node whose average power consumption would be 100 µW, over a frequency bandwidth as large as 21% of the central frequency (the bandwidth classically defined at half of the maximal power is equal to 17.8%). It is worth noting that the bandwidth obtained with the PSSECE circuit is larger than the ones obtained in section 4.4 with a simple resistive tuning, which confirm the superior performance of this circuit in this area, as described in [33]. The overall consumption of the PSSECE circuit is typically below 1 µW, which remains negligible compared to the harvested power.

Our strongly coupled prototype, leveraged by the tunable PSSECE circuit, exhibits a wide harvesting bandwidth while the resonant frequency tuning subsystem consumes only a negligible part of the extracted power.

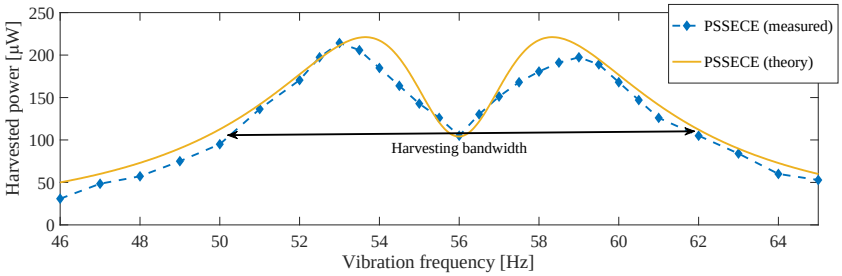

Figure 20: Harvested power with our prototype connected to the PSSECE circuit for vibration frequencies ranging from 46Hz to 65Hz. The yellow line is the theoretical prediction obtained from [35] multiplied by a 85% factor corresponding to the typical efficiency of the PSSECE circuit [12]. Blue diamonds correspond to experimental measurements realized with our prototype and the PSSECE circuit.

5. Conclusion

This paper reports a method to design piezoelectric cantilevers with strong electromechanical coupling coefficients k^2. Such harvesters allow broadband vibration energy harvesting when combined with resonant frequency tuning electrical techniques. An analytical model, based on the Rayleigh-Ritz method and a new two degrees-of-freedom model, is proposed and validated through a comparison with FEM simulations. A new analytical expression of the alternative electromechanical coupling coefficient is deduced from the model and proves to be effective to give design guidelines. The major findings are:

- The longitudinal and transverse stress distributions can be optimized separately as they do not depend on the same parameters.
- k^2 increases with the ratio between the rotary inertia of the proof mass and its mass.
- Cantilevers with long proof masses are effective configurations to maximize k^2.
- Wide beams based on PZT ceramic materials exhibit larger k^2 than narrow beams.

The design guidelines are validated by PMN-PT and PZT based prototypes that present equal resonant frequencies (≈ 30Hz). The fabricated cantilevers exhibit some of the best k^2 reported for such materials: 16.6% and 11.3% for the narrow PMN-PT and PZT-5A prototypes respectively and 16.4% for the wide PZT-5A prototype. The wide prototype's k^2 represents a 45% increase compared to the narrow PZT-based prototype, and a 31% increase compared to the reported literature on PZT-based cantilevers. Power measurements show that the prototypes exhibit very high normalized power densities and wide bandwidth behaviors on an optimal resistive load: 10.1%, 7.8% and 11.3% of the central frequency for the narrow PMN-PT cantilever, narrow PZT cantilever and wide PZT cantilever, respectively. To illustrate the potential applications of such generators, we describe a strongly coupled prototype dedicated to HVAC environment, leveraged by a dedicated integrated circuit integrating the PSSECE technique able to tune the resonant frequency of the generator. This device harvests more than 100 µW over a 21% frequency band. The resonant frequency management circuit consumes less than 1 µW and the harvested power is sufficient to supply a low power WSN. Moreover, we experimentally demonstrate that the harvester recovers its optimal performance even shortly after wide frequency variations.

The bandwidths provided by our approach are sufficient to address issues in many real-world applications where the ambient vibration frequency varies and/or where the resonant frequency of the harvester drifts due to temperature variations or aging. The strongly coupled harvesters proposed in this work, coupled to resonant frequency tuning techniques, pave the way toward the development of autonomous sensors self-adjustable to sensitive change in the operating environment.

References

[1] Torah R, Glynne-Jones P, Tudor M, O'Donnell T, Roy S, Beeby S. Self-powered autonomous wireless sensor node using vibration energy harvesting. Meas Sci Technol 2008;19:125202. https://doi.org/10.1088/0957-0233/19/12/125202.

[2] Roundy SJ. Energy scavenging for wireless sensor nodes with a focus on vibration to electricity conversion. PhD Thesis. University of California, Berkeley Berkeley, CA, 2003.

[3] Tang L, Yang Y, Soh CK. Toward Broadband Vibration-based Energy Harvesting. J Intell Mater Syst Struct 2010;21:1867–97. https://doi.org/10.1177/1045389X10390249.

[4] Neri I, Travasso F, Mincigrucci R, Vocca H, Orfei F, Gammaitoni L. A real vibration database for kinetic energy harvesting application. J Intell Mater Syst Struct 2012;23:2095–101. https://doi.org/10.1177/1045389X12444488.

[5] Rantz R, Roundy S. Characterization of real-world vibration sources with a view toward optimal energy harvesting architectures. Ind. Commer. Appl. Smart Struct. Technol. 2016, vol. 9801, International Society for Optics and Photonics; 2016, p. 98010P. https://doi.org/10.1117/12.2219416.

[6] Hoang T, Ferin G, Bantignies C, Rosinski B, Vince P, Cheppe M, et al. Accelerated Aging Procedures of Bending Piezoelectric Structures Using Electrical Stress Induced Approaches. 2018 IEEE Int. Ultrason. Symp. IUS, 2018, p. 1–4. https://doi.org/10.1109/ULTSYM.2018.8579799.

[7] Kuo YC, Chien JT, Shih WT, Chen CT, Lin SC, Wu WJ. The fatigue behavior study of micro piezoelectric energy harvester under different working temperature. Act. Passive Smart Struct. Integr. Syst. XIII, vol. 10967, International Society for Optics and Photonics; 2019, p. 109672H. https://doi.org/10.1117/12.2514427.

[8] Gasnier P, Boucaud M, Gallardo M, Willemin J, Boisseau S, Morel A, et al. A 120°C 20G-compliant vibration energy harvester for aeronautic environments. J Phys Conf Ser 2019;1407:012118. https://doi.org/10.1088/1742-6596/1407/1/012118.

[9] Brenes A, Morel A, Gibus D, Yoo C-S, Gasnier P, Lefeuvre E, et al. Large-bandwidth piezoelectric energy harvesting with frequency-tuning synchronized electric charge extraction. Sens Actuators Phys 2020;302:111759. https://doi.org/10.1016/j.sna.2019.111759.

[10] Morel A, Pillonnet G, Gasnier P, Lefeuvre E, Badel A. Frequency tuning of piezoelectric energy harvesters thanks to a short-circuit synchronous electric charge extraction. Smart Mater Struct 2018;28:025009. https://doi.org/10.1088/1361-665X/aaf0ea.

[11] Cai Y, Manoli Y. A piezoelectric energy-harvesting interface circuit with fully autonomous conjugate impedance matching, 156% extended bandwidth, and 0.38μW power consumption. 2018 IEEE Int. Solid - State Circuits Conf. - ISSCC, 2018, p. 148–50. https://doi.org/10.1109/ISSCC.2018.8310227.

[12] Morel A, Quelen A, Berlitz CA, Gibus D, Gasnier P, Badel A, et al. 32.2 Self-Tunable Phase-Shifted SECE Piezoelectric Energy-Harvesting IC with a 30nW MPPT Achieving 446% Energy-Bandwidth Improvement and 94% Efficiency. 2020 IEEE Int. Solid- State Circuits Conf. - ISSCC, 2020, p. 488–90. https://doi.org/10.1109/ISSCC19947.2020.9062972.

[13] Pradeesh EL, Udhayakumar S. Effect of placement of piezoelectric material and proof mass on the performance of piezoelectric energy harvester. Mech Syst Signal Process 2019;130:664–76. https://doi.org/10.1016/j.ymssp.2019.05.044.

[14] Tran N, Ghayesh MH, Arjomandi M. Ambient vibration energy harvesters: A review on nonlinear techniques for performance enhancement. Int J Eng Sci 2018;127:162–85. https://doi.org/10.1016/j.ijengsci.2018.02.003.

[15] Huguet T, Badel A, Druet O, Lallart M. Drastic bandwidth enhancement of bistable energy harvesters: Study of subharmonic behaviors and their stability robustness. Appl Energy 2018;226:607–17. https://doi.org/10.1016/j.apenergy.2018.06.011.

[16] Mažeika D, Čeponis A, Vasiljev P, Borodinas S, Pliuskuvienė B. Saw-tooth type piezoelectric multi-modal energy harvester. Sens Actuators Phys 2019;288:125–33. https://doi.org/10.1016/j.sna.2019.02.009.

[17] Wu W-J, Chen Y-Y, Lee B-S, He J-J, Peng Y-T. Tunable resonant frequency power harvesting devices. In: Clark WW, Ahmadian M, Lumsdaine A, editors., San Diego, CA: 2006, p. 61690A. https://doi.org/10.1117/12.658546.

[18] Zhao S, Radhakrishna U, Hanly S, Ma J, Lang JH, Buss D. Co-optimization of a piezoelectric energy harvesting system for broadband operation. J Phys Conf Ser 2019;1407:012010. https://doi.org/10.1088/1742-6596/1407/1/012010.
[19] Seddik BA, Despesse G, Defay E. Wideband mechanical energy harvester based on piezoelectric longitudinal mode. New Circuits Syst. Conf. NEWCAS 2012 IEEE 10th Int., IEEE; 2012, p. 453–456.
[20] Ahmed-Seddik B, Despesse G, Boisseau S, Defay E. Self-powered resonant frequency tuning for Piezoelectric Vibration Energy Harvesters. J Phys Conf Ser 2013;476:012069. https://doi.org/10.1088/1742-6596/476/1/012069.
[21] Badel A, Lefeuvre E. Wideband Piezoelectric Energy Harvester Tuned Through its Electronic Interface Circuit. J Phys Conf Ser 2014;557:012115. https://doi.org/10.1088/1742-6596/557/1/012115.
[22] Kim M, Hoegen M, Dugundji J, Wardle BL. Modeling and experimental verification of proof mass effects on vibration energy harvester performance. Smart Mater Struct 2010;19:045023. https://doi.org/10.1088/0964-1726/19/4/045023.
[23] Yang Z, Zu J. Comparison of PZN-PT, PMN-PT single crystals and PZT ceramic for vibration energy harvesting. Energy Convers Manag 2016;122:321–9. https://doi.org/10.1016/j.enconman.2016.05.085.
[24] Xiong X, Oyadiji SO. Modal electromechanical optimization of cantilevered piezoelectric vibration energy harvesters by geometric variation. J Intell Mater Syst Struct 2014;25:1177–95. https://doi.org/10.1177/1045389X13502872.
[25] Jia Y, Seshia AA. Power Optimization by Mass Tuning for MEMS Piezoelectric Cantilever Vibration Energy Harvesting. J Microelectromechanical Syst 2016;25:108–17. https://doi.org/10.1109/JMEMS.2015.2496346.
[26] Wang Q-M, Du X-H, Xu B, Cross LE. Electromechanical coupling and output efficiency of piezoelectric bending actuators. IEEE Trans Ultrason Ferroelectr Freq Control 1999;46:638–646.
[27] Ng TH, Liao WH. Sensitivity Analysis and Energy Harvesting for a Self-Powered Piezoelectric Sensor. J Intell Mater Syst Struct 2005;16:785–97. https://doi.org/10.1177/1045389X05053151.
[28] Yu S, He S, Li W. Theoretical and experimental studies of beam bimorph piezoelectric power harvesters. J Mech Mater Struct 2010;5:427–45. https://doi.org/10.2140/jomms.2010.5.427.
[29] Gibus D, Gasnier P, Morel A, Boisseau S, Badel A. Modelling and design of highly coupled piezoelectric energy harvesters for broadband applications. J Phys Conf Ser 2019;1407:012009. https://doi.org/10.1088/1742-6596/1407/1/012009.
[30] Lei A, Xu R, Borregaard LM, Guizzetti M, Hansen O, Thomsen EV. Impedance Based Characterization of a High-Coupled Screen Printed PZT Thick Film Unimorph Energy Harvester. J Microelectromechanical Syst 2014;23:842–54. https://doi.org/10.1109/JMEMS.2013.2295625.
[31] Choudhary V, Iniewski K. MEMS: Fundamental Technology and Applications. CRC Press; 2017.
[32] Dutoit NE, Wardle BL, Kim S-G. DESIGN CONSIDERATIONS FOR MEMS-SCALE PIEZOELECTRIC MECHANICAL VIBRATION ENERGY HARVESTERS. Integr Ferroelectr 2005;71:121–60. https://doi.org/10.1080/10584580590964574.
[33] Badel A, Lefeuvre E. Nonlinear Conditioning Circuits for Piezoelectric Energy Harvesters. In: Blokhina E, El Aroudi A, Alarcon E, Galayko D, editors. Nonlinearity Energy Harvest. Syst. Micro- Nanoscale Appl., Cham: Springer International Publishing; 2016, p. 321–59. https://doi.org/10.1007/978-3-319-20355-3_10.
[34] Morel A, Badel A, Grézaud R, Gasnier P, Despesse G, Pillonnet G. Resistive and reactive loads' influences on highly coupled piezoelectric generators for wideband vibrations energy harvesting. J Intell Mater Syst Struct 2019;30:386–99. https://doi.org/10.1177/1045389X18810802.
[35] Lefeuvre E, Badel A, Brenes A, Seok S, Yoo C-S. Power and frequency bandwidth improvement of piezoelectric energy harvesting devices using phase-shifted synchronous electric charge extraction interface circuit. J Intell Mater Syst Struct 2017;28:2988–95. https://doi.org/10.1177/1045389X17704914.
[36] Hagood NW, Chung WH, Von Flotow A. Modelling of piezoelectric actuator dynamics for active structural control. J Intell Mater Syst Struct 1990;1:327–354.
[37] Tadmor EB, Kosa G. Electromechanical coupling correction for piezoelectric layered beams. J Microelectromechanical Syst 2003;12:899–906. https://doi.org/10.1109/JMEMS.2003.820286.
[38] Kim M. Materials and device design for MEMS piezoelectric mechanical vibration energy harvesters. PhD Thesis. Massachusetts Institute of Technology, 2012.
[39] Oguamanam DCD. Free vibration of beams with finite mass rigid tip load and flexural–torsional coupling. Int J Mech Sci 2003;45:963–79. https://doi.org/10.1016/j.ijmecsci.2003.09.014.
[40] Gong LJ, Pan CL, Pan QS, Feng ZH. Theoretical analysis of dynamic property for piezoelectric cantilever triple-layer benders with large piezoelectric and electromechanical coupling coefficients. J Adv Dielectr 2016;06:1650017. https://doi.org/10.1142/S2010135X1650017X.

[41] Erturk A, Tarazaga PA, Farmer JR, Inman DJ. Effect of Strain Nodes and Electrode Configuration on Piezoelectric Energy Harvesting From Cantilevered Beams. J Vib Acoust 2009;131:011010. https://doi.org/10.1115/1.2981094.
[42] Ducarne J, Thomas O, Deü J-F. Placement and dimension optimization of shunted piezoelectric patches for vibration reduction. J Sound Vib 2012;331:3286–303. https://doi.org/10.1016/j.jsv.2012.03.002.
[43] Chen C, Zhang R, Wang Z, Cao W. Electromechanical coupling coefficient k31eff for arbitrary aspect ratio resonators made of [001] and [011] poled (1−x)Pb(Mg1/3Nb2/3)O3–xPbTiO3 single crystals. J Appl Phys 2009;105:064104. https://doi.org/10.1063/1.3086653.
[44] The Institute of Electrical and Electronics Engineers. IEEE Standard on Piezoelectricity. ANSIIEEE Std 176-1987 1988. https://doi.org/10.1109/IEEESTD.1988.79638.
[45] TRS Technologies, Inc. Http://WwwTrstechnologiesCom/Resources n.d. http://www.trstechnologies.com/Resources (accessed September 19, 2018).
[46] Noliac piezoceramic material NCE51. Noliac - Your Piezo Partn n.d. http://www.noliac.com/products/materials/nce51/ (accessed October 16, 2019).
[47] Kim JE, Kim YY. Analysis of Piezoelectric Energy Harvesters of a Moderate Aspect Ratio With a Distributed Tip Mass. J Vib Acoust 2011;133:041010. https://doi.org/10.1115/1.4003598.
[48] Curatolo M, La Rosa M, Prestininzi P. On the validity of plane state assumptions in the bending of bimorph piezoelectric cantilevers. J Intell Mater Syst Struct 2019:1045389X1983595. https://doi.org/10.1177/1045389X19835959.
[49] Morel A, Grézaud R, Pillonnet G, Gasnier P, Despesse G, Badel A. Active AC/DC control for wideband piezoelectric energy harvesting. J Phys Conf Ser 2016;773:012059. https://doi.org/10.1088/1742-6596/773/1/012059.
[50] Tang G, Yang B, Liu J, Xu B, Zhu H, Yang C. Development of high performance piezoelectric d33 mode MEMS vibration energy harvester based on PMN-PT single crystal thick film. Sens Actuators Phys 2014;205:150–5. https://doi.org/10.1016/j.sna.2013.11.007.
[51] Siddiqui NA, Kim D-J, Overfelt RA, Prorok BC. Electromechanical coupling effects in tapered piezoelectric bimorphs for vibration energy harvesting. Microsyst Technol 2017;23:1537–51. https://doi.org/10.1007/s00542-016-3197-4.
[52] Beeby SP, Torah RN, Tudor MJ, Glynne-Jones P, O\textquotesingleDonnell T, Saha CR, et al. A micro electromagnetic generator for vibration energy harvesting. J Micromechanics Microengineering 2007;17:1257–1265. https://doi.org/10.1088/0960-1317/17/7/007.
[53] Leadenham S, Erturk A. Unified nonlinear electroelastic dynamics of a bimorph piezoelectric cantilever for energy harvesting, sensing, and actuation. Nonlinear Dyn 2015;79:1727–43. https://doi.org/10.1007/s11071-014-1770-x.
[54] Jackson N, Olszewski OZ, O'Murchu C, Mathewson A. Shock-induced aluminum nitride based MEMS energy harvester to power a leadless pacemaker. Sens Actuators Phys 2017;264:212–8. https://doi.org/10.1016/j.sna.2017.08.005.
[55] Yang Z, Zhou S, Zu J, Inman D. High-Performance Piezoelectric Energy Harvesters and Their Applications. Joule 2018.
[56] Beeby SP, Wang L, Zhu D, Weddell AS, Merrett GV, Stark B, et al. A comparison of power output from linear and nonlinear kinetic energy harvesters using real vibration data. Smart Mater Struct 2013;22:075022. https://doi.org/10.1088/0964-1726/22/7/075022.
[57] Wozniak MV, Conlon SC, Smith EC, Reichard KM. Design, Analysis, and Characterization of Single Crystal Energy Harvesters for Rotorcraft Wireless Sensor Applications 2015. https://doi.org/info:doi/10.4050/JAHS.60.022006.
[58] Benchemoul M, Ferin G, Rosinski B, Bantignies C, Hoang T, Vince P, et al. Wireless Inertial Sensing Platform Self-Powered by Piezoelectric Energy Harvester for Industrial Predictive Maintenance. 2018 IEEE Int. Ultrason. Symp. IUS, 2018, p. 1–4. https://doi.org/10.1109/ULTSYM.2018.8580029.
[59] Roundy S, Wright PK, Rabaey J. A study of low level vibrations as a power source for wireless sensor nodes. Comput Commun 2003;26:1131–1144.
[60] Lefeuvre E, Badel A, Richard C, Guyomar D. Piezoelectric Energy Harvesting Device Optimization by Synchronous Electric Charge Extraction. J Intell Mater Syst Struct 2005;16:865–76. https://doi.org/10.1177/1045389X05056859.

Appendix A

Modeling a piezoelectric cantilever can be done with any shape of proof mass. We can consider that the gravity center of the proof mass O is at a distance D_t and H_t according to O_x and O_z directions. If I_o is the rotary inertia of the proof mass according to its gravity center O, we can compute the rotary inertia I_t according to the projection on the neutral axis thanks to the Huygens theorem (62).

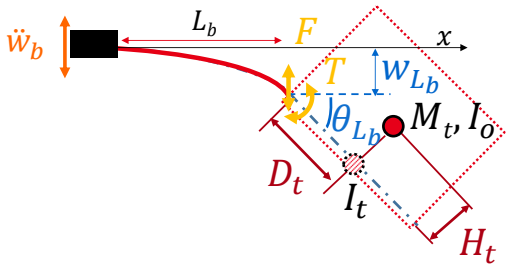

Figure 21: Cantilever with an asymetric proof mass

$$I_t = I_o + H_t^2 M_t \tag{62}$$

Appendix B

Finding the resonant pulsations of the system in (42) is done by finding the roots of the determinant of the matrix (63). The solutions are given in (64) and (65). They represent the short circuit resonant angular frequencies of a piezoelectric cantilever with a proof mass when the beam mass is neglected.

$$det\left(\omega^2 \begin{bmatrix} M_t & D_t M_t \\ D M_t & I_t + D_t^2 M_t \end{bmatrix} + \frac{YI}{L_b^2} \begin{bmatrix} \frac{12}{L_b} & -6 \\ -6 & 4L_b \end{bmatrix}\right) = 0 \tag{63}$$

$$\omega_1^2 = \frac{2\,YI\left(3\,I_t - \sqrt{(9\,D_t^4 M_t^2 + 18\,D_t^3 L_b M_t^2 + 18\,D_t^2 I_t M_t + 15\,D_t^2 L_b^2 M_t^2 + 18\,D_t\,I_t L_b M_t + 6\,D_t\,L_b^3 M_t^2 + 9\,I_t^2 + 3\,I_t L_b^2 M_t + L_b^4 M_t^2)} + 3\,D_t^2 M_t + L_b^2 M_t + 3\,D_t\,L_b M_t\right)}{I_t L_b^3 M_t} \tag{64}$$

$$\omega_2^2 = \frac{2\,YI\left(3\,I_t + \sqrt{(9\,D_t^4 M_t^2 + 18\,D_t^3 L_b M_t^2 + 18\,D_t^2 I_t M_t + 15\,D_t^2 L_b^2 M_t^2 + 18\,D_t\,I_t L_b M_t + 6\,D_t\,L_b^3 M_t^2 + 9\,I_t^2 + 3\,I_t L_b^2 M_t + L_b^4 M_t^2)} + 3\,D_t^2 M_t + L_b^2 M_t + 3\,D_t\,L_b M_t\right)}{I_t L_b^3 M_t} \tag{65}$$